https://doi.org/10.5194/egusphere-2026-5154
Preprint. Discussion started: 2 November 2026
© Author(s) 2026. CC BY 4.0 License.

Task-dependent timing admissibility in digital seismology: forward propagation of structured timing errors into phase, polarisation, and array measurements

Antonino D'Alessandro
Istituto Nazionale di Geofisica e Vulcanologia, Osservatorio Nazionale Terremoti, Rome, Italy
antonino.dalessandro@ingv.it
https://orcid.org/0000-0002-0074-3125

Abstract

Accurate timing is essential in digital seismology, yet a single clock-accuracy specification does not determine whether a recording system is adequate for a given seismic measurement. Here I formulate timing quality as a task-dependent admissibility problem in which the temporal evolution, spatial or channel topology, and covariance of timing errors are propagated through the measurement operator of the observable of interest. Analytical and numerical formulations are developed for spectral phase, differential delay, three-component polarisation, array slowness and backazimuth, and coherent beamforming. The framework distinguishes absolute, differential, intercomponent, spatially structured, and common-mode timing errors and expresses admissibility through deterministic or probabilistic performance criteria. Controlled synthetic experiments, a perturbation benchmark using a public three-component seismic waveform, and a controlled benchmark based on a public compact-array geometry demonstrate that nominally identical timing uncertainties can produce markedly different measurement errors. At 10 Hz, a 95 % single-path phase criterion of 15° admits a timing standard deviation of approximately 2.13 ms, whereas corresponding representative benchmark limits are approximately 6.44 ms for intercomponent polarisation and 2.99 ms for compact-array backazimuth; an independent-error beam-coherence criterion $C_B \geq 0.90$ gives approximately 5.17 ms. These values are not interchangeable specifications because they act on different timing-error variables. Timing covariance is equally important: common-mode errors can cancel from relative observables, whereas differential errors remain observable, and spatially linear timing gradients can be indistinguishable from slowness perturbations under a plane-wave model. Extension to empirically estimated, non-Gaussian, and non-stationary clock processes would allow the same framework to support operational task-specific timing assessment. The results show that timing performance should be evaluated forward from the structured timing process to the intended seismic observable, rather than inferred from a universal millisecond threshold.

1 Introduction

Accurate timing is a fundamental requirement of digital seismology because the temporal coordinate assigned to each sample enters directly into the estimation of phase, travel time, waveform coherence, particle motion, and spatial wavefield structure. The importance of timekeeping has accompanied instrumental seismology throughout its development, although the technologies used to establish and transfer time have evolved from local clocks and manual corrections to satellite-disciplined digital acquisition systems (Agnew, 2020). Modern permanent stations commonly discipline their acquisition clocks using Global Navigation Satellite System (GNSS) timing, and network-level timing quality is routinely monitored as an integral component of seismic data quality (Ringler et al., 2021). Autonomous instruments present a more difficult case. In particular, ocean-bottom seismometers (OBSs) cannot normally maintain GNSS synchronisation during deployment and must rely on local oscillators whose offsets and drift are estimated after recovery (Hannemann et al., 2014; Cabieces et al., 2024; Schmidt-Aursch et al., 2026). Timing problems are nevertheless not restricted to autonomous deployments: large-scale evaluations of permanent global and regional networks have identified timing anomalies ranging from tens of milliseconds to seconds, demonstrating that synchronisation remains a practical issue even in mature digital networks (Ringler et al., 2021; Yang et al., 2022).

The effect of an imperfect clock cannot, however, be characterised adequately by a single undifferentiated notion of "timing accuracy". A timing-error process may contain a deterministic offset, a fractional-frequency error, stochastic fluctuations, nonlinear drift, and discrete jumps, each having a different temporal structure. Oscillator stability is conventionally characterised using quantities such as the Allan variance or Allan deviation, whose averaging-time dependence distinguishes different frequency-noise processes (Allan, 1966). In distributed seismic acquisition, an additional distinction is required between perturbations that are common

https://doi.org/10.5194/egusphere-2026-5154
Preprint. Discussion started: 2 November 2026
© Author(s) 2026. CC BY 4.0 License.

to an entire system, perturbations that differ among stations, and residual delays that differ among channels nominally recorded synchronously. Consequently, the amplitude of a timing perturbation alone does not determine its effect on a seismic measurement. Its temporal evolution, spatial or channel covariance, and relationship to the measurement operator are equally important.

A substantial body of work has therefore focused on identifying, documenting, estimating, and correcting timing errors in seismic data. Timing inconsistencies have been recognised through direct waveform and metadata diagnostics at permanent stations (Gibbons, 2006; Weidle et al., 2013), through systematic analysis of travel-time residuals (Syracuse et al., 2017), and through large-scale network assessments (Ringler et al., 2021; Yang et al., 2022). Ambient-noise interferometry provided an especially important development because repeated cross-correlations can reveal instrumental time shifts without an external timing reference (Stehly et al., 2007; Sens-Schönfelder, 2008). This approach has been extended to OBS deployments to estimate static offsets and drift rates (Hannemann et al., 2014), correct instrumental clock errors (Gouédard et al., 2014), and obtain high-accuracy timing estimates from multiple components and frequency bands (Hable et al., 2018; Tian et al., 2021). More recent applications include large-N arrays (Weemstra et al., 2021), continuous monitoring of volcanic networks (Hirose and Ueda, 2023), dense-array phase-delay analysis (Lecointre et al., 2023), large-aperture OBS networks (Cabieces et al., 2024), explicitly nonlinear OBS clock drift (Schmidt-Aursch et al., 2026), and wavefield-domain refinement of residual timing errors remaining after hardware synchronisation (Song et al., 2026). Collectively, these studies establish timing recovery as an important inverse and quality-control problem in modern seismology.

Application-specific consequences of timing errors have also been examined in individual contexts. Arrival-time errors, for example, propagate into traveltime tomography and can map into errors or blurring of the inferred velocity structure (Röhm et al., 2000). In array processing, timing and phase inconsistencies alter inter-station phase alignment and can be estimated from the resulting phase-delay structure (Weemstra et al., 2021; Lecointre et al., 2023). Network-level studies similarly assess whether measured timing performance is adequate for particular classes of seismic observations (Ringler et al., 2021). These studies are important precedents, but they generally address either the detection and recovery of timing errors or their consequences within a specific analysis. The complementary forward problem has received substantially less systematic treatment: given a structured timing-error process with specified bias, variance, covariance, and temporal behaviour, how does it propagate into the error of a particular seismic observable, and what residual timing performance is admissible for a prescribed scientific task?

This distinction is consequential because timing perturbations having the same nominal amplitude can produce fundamentally different measurement errors. A constant timing offset produces a spectral phase shift proportional to frequency, yet cancels from a perfectly differential delay when the same offset is shared by both signals. A common time translation applied synchronously to all three components leaves their intrinsic zero-lag polarisation covariance unchanged, apart from finite-window selection effects in non-stationary waveforms, whereas a relative inter-channel delay can substantially alter the estimated principal direction. For an array, a timing offset common to all stations can be absorbed into the origin-time intercept, while a spatially varying timing field can project directly into the estimated slowness vector. A linear spatial timing gradient is, in fact, formally indistinguishable from a corresponding slowness perturbation under a plane-wave model. Likewise, coherent beamforming depends principally on pairwise timing differences, so that its degradation is governed by the covariance of the timing field rather than by the marginal variance of individual station clocks alone. These examples show why a universal requirement expressed only as a single maximum timing error or timing standard deviation is generally insufficient.

The problem is becoming increasingly relevant as seismic acquisition systems become more heterogeneous. Contemporary observing systems combine broadband seismometers, strong-motion sensors, compact MicroElectroMechanical-System (MEMS) devices, autonomous nodes, multi-channel digitizers, cabled observatories, and dense arrays, often with different clock architectures, sampling rates, digital filters, telemetry paths, and metadata conventions. Reviews of global broadband instrumentation and modern seismic digitisation emphasise that measurement quality depends on the complete acquisition chain rather than on the mechanical sensor alone (Ringler et al., 2022, 2023). Recent causal and uncertainty-aware formulations have similarly shown that geoscientific instrument performance must be considered together with discretisation, digital filtering, self-noise, parameter uncertainty, and physically realisable acquisition chains (D'Alessandro, 2026a, b). Timing constitutes a distinct but complementary dimension of this problem: even when amplitude response and instrumental noise are adequately characterised, the scientific usefulness of the waveform may still depend on whether its timing structure is compatible with the downstream measurement task.

https://doi.org/10.5194/egusphere-2026-5154
Preprint. Discussion started: 2 November 2026
© Author(s) 2026. CC BY 4.0 License.

In this study, I formulate seismic timing quality as a task-dependent measurement-admissibility problem rather than as a universal scalar property of the recorder clock. The relevant question is not whether a timing perturbation is intrinsically "small" or "large", but whether its forward propagation keeps a specified measurement error within an accepted performance criterion. The framework therefore links four elements that are commonly treated separately: the metrological description and temporal evolution of the timing-error process, its spatial or channel covariance structure, the forward operator associated with the seismic measurement, and a task-specific admissibility criterion. Common-mode, inter-station, and inter-channel timing perturbations are treated as distinct spatial or channel topologies, while deterministic offset, fractional-frequency error, stochastic timing fluctuations, drift, and jumps are distinguished as different temporal processes.

The study makes five main contributions. First, I establish a metrologically explicit description of timing error, systematic or mean timing components, uncertainty, covariance, and clock stability for seismic acquisition systems. Second, I derive the forward propagation of timing perturbations into spectral phase, differential delay, three-component polarisation, array slowness and backazimuth, and coherent beamforming. Third, I show analytically that several apparently general timing requirements are conditional on timing topology: constant common-mode offsets cancel from some differential observables, whereas relative intercomponent timing errors, spatial timing gradients, and imperfectly correlated station errors do not. Fourth, I formulate timing admissibility probabilistically so that acceptable timing performance can be expressed as a bound conditioned on frequency, array geometry, timing covariance, wavefield properties, and analysis settings. Fifth, I evaluate these relations through controlled synthetic experiments, a controlled perturbation of a public observational three-component waveform example, and a public array-geometry benchmark, complemented by robustness analyses of timing-error distributions, fractional-delay and sampling implementation, array geometry, common-versus-differential timing structure, observational processing choices, and timing–position–propagation identifiability.

The objective is therefore not to introduce another algorithm for detecting or correcting clock drift. Rather, the study addresses the complementary question of what residual timing uncertainty means for the scientific measurement after synchronisation, quality control, or correction has been attempted. Although application-specific effects of timing errors have been considered in individual seismic analyses, existing timing studies have predominantly emphasised detection, estimation, or correction of instrumental clock errors. To my knowledge, a unified forward framework that maps structured timing uncertainty into task-specific performance bounds across phase, polarisation, slowness/backazimuth, and coherent array observables has not been developed. The resulting formulation is intended to provide a quantitative bridge between instrument timing specifications and the actual performance requirements of seismic analyses, while explicitly identifying the conditions under which timing errors cancel, remain observable, or become confounded with other sources of measurement uncertainty.

The remainder of the paper is organised as follows. Sect. 2 develops the metrological framework and distinguishes the spatial and temporal structures of timing errors. Sect. 3 derives their forward propagation into seismic observables and defines task-dependent timing admissibility. Sect. 4 describes the synthetic, observational, and array benchmarks and the associated numerical procedures. Sect. 5 presents frequency-, geometry-, covariance-, and task-dependent performance limits. Sect. 6 discusses the implications for seismic instrumentation, timing metadata, common-mode invariance, and identifiability with non-timing errors. Sect. 7 summarises the main conclusions.

2 Metrological framework for structured timing errors

A rigorous treatment of seismic timing requires a clear distinction between realised timing error, systematic or mean components of that error, stochastic variability, and uncertainty concerning its value. According to the International Vocabulary of Metrology (VIM), measurement error and measurement uncertainty are distinct concepts, whereas measurement accuracy is qualitative and should not be used as a numerical synonym for either error or uncertainty (JCGM, 2012). Let t_{obs} denote the time assigned by the acquisition system to a sample or measurement event and t_{ref} the corresponding reference time. I define the realised timing error as

$$\delta t = t_{\mathrm{obs}} - t_{\mathrm{ref}}. \qquad (1)$$

https://doi.org/10.5194/egusphere-2026-5154
Preprint. Discussion started: 2 November 2026
© Author(s) 2026. CC BY 4.0 License.

According to this convention, $\delta t > 0$ indicates that the assigned timestamp is later than the adopted reference time. Equation (1) describes a realised deviation and does not itself constitute an uncertainty statement. Measurement uncertainty instead quantifies the dispersion of values that can reasonably be attributed to the measurand on the basis of the information available (JCGM, 2008a, 2012).

At a specified epoch, or over an explicitly defined statistical ensemble, the timing error may be represented as

$$\delta t = b_t + \epsilon_t, \qquad b_t = \mathbb{E}[\delta t], \qquad \mathbb{E}[\epsilon_t] = 0, \tag{2}$$

with variance

$$\sigma_t^2 = \mathrm{Var}(\delta t) = \mathbb{E}\left[(\delta t - b_t)^2\right]. \tag{3}$$

Here, b_t denotes the ensemble-mean timing error. When the ensemble represents repeated measurements under specified conditions, this mean may estimate a systematic timing-error component, but it is not used as a generic synonym for the VIM quantity measurement bias. Likewise, σ_t denotes the standard deviation of the specified timing-error ensemble and is not a numerical definition of clock accuracy. The same probability distribution may have two conceptually different interpretations: it may describe physical realisation-to-realisation variability of a stochastic timing process, or state-of-knowledge uncertainty concerning an incompletely known residual timing error. In the latter case, its standard deviation can be interpreted as a standard uncertainty. These interpretations are kept distinct when probabilities are assigned to downstream measurement performance.

This distinction becomes particularly important after clock correction. If an estimated correction is applied, the quantity relevant to subsequent measurement is the residual timing error rather than the original clock deviation. Its uncertainty may contain contributions from uncertainty in the estimated correction, unmodelled systematic effects, and subsequent clock variability. The physical residual timing error perturbs the waveform, whereas measurement uncertainty describes incomplete knowledge of that perturbation. Timing quantities are therefore treated below as inputs to a measurement model and propagated to derived seismic quantities following the general framework of the GUM and GUM-6 (JCGM, 2008a, 2020).

Let t_r denote reference time and let $\mathcal{T}_{ic}$ denote the mapping from reference time to the time assigned by the acquisition system for station i and channel c. The exact clock-time mapping is

$$\mathcal{T}_{ic}(t_\mathrm{r}) \equiv t_{ic}(t_\mathrm{r}) = t_\mathrm{r} + \delta t_{ic}(t_\mathrm{r}). \tag{4}$$

On intervals over which this mapping is monotonic and therefore invertible, the recorded trace indexed by assigned time t is

$$d_{ic}(t) = s_{ic}\left[\mathcal{T}_{ic}^{-1}(t)\right] + n_{ic}(t), \tag{5}$$

where $s_{ic}(t_\mathrm{r})$ is the ideal continuous-time seismic signal expressed on the reference time scale and $n_{ic}(t)$ represents additive measurement noise and other residual disturbances not explicitly attributed to timing.

For a constant timing error, the inverse mapping reduces exactly to a time translation. For a sufficiently small and slowly varying timing error, the inverse mapping can be approximated locally by $\mathcal{T}_{ic}^{-1}(t) \simeq t - \delta t_{ic}(t)$, giving

$$d_{ic}(t) \simeq s_{ic}\left[t - \delta t_{ic}(t)\right] + n_{ic}(t). \tag{6}$$

For a differentiable signal and sufficiently small δt_{ic}, first-order expansion gives

$$d_{ic}(t) - s_{ic}(t) \simeq -\delta t_{ic}(t)\frac{\mathrm{d}s_{ic}(t)}{\mathrm{d}t} + n_{ic}(t). \tag{7}$$

Equation (7) provides the simplest local explanation for the frequency dependence of timing sensitivity: for a fixed timing perturbation, waveform error increases with the temporal gradient of the signal. This linearisation is used only for interpretation. The numerical experiments introduced later apply finite timing perturbations

https://doi.org/10.5194/egusphere-2026-5154
Preprint. Discussion started: 2 November 2026
© Author(s) 2026. CC BY 4.0 License.

directly and do not rely on Eq. (7). When the clock mapping contains discrete jumps, the inverse-time representation is instead treated piecewise on intervals over which the mapping remains well defined.

Clock timing must also be distinguished from deterministic latency elsewhere in the acquisition chain. Sensors, analogue anti-alias stages, digitiser pipelines, digital filters, decimation stages, telemetry systems, and resampling procedures can all introduce temporal or phase effects. A general frequency-dependent instrumental phase response is not equivalent to a scalar clock error. Only a pure delay, fixed channel latency, or approximately constant group delay over the analysed frequency band can be represented as an effective timing offset. Other frequency-dependent effects remain part of the instrument-response model. Accordingly, δt_{ic} denotes here the residual effective timing perturbation relevant to the seismic measurement after known deterministic acquisition delays have been accounted for.

The measurement consequence of a timing perturbation depends not only on its magnitude but also on how it is shared among the stations and channels contributing to the observable. I represent the effective timing error at station $i$and channel c as

$$\delta t_{ic}(t) = \delta t_{\mathrm{net}}(t) + \delta t_i(t) + \delta t_{ic}^{\mathrm{ch}}(t), \qquad (8)$$

where δt_{net} is common to the acquisition system or network under consideration, δt_i is a station-specific contribution shared by the relevant channels of station i, and $\delta t_{ic}^{\mathrm{ch}}$ is a residual channel-dependent contribution. Equation (8) is a conceptual topological decomposition rather than an assumption of statistical independence. Its terms may be correlated, and their covariance must be retained whenever those correlations affect the measurement.

The decomposition is not unique if its individual terms are to be inferred from observations. A constant contribution can, for example, be transferred between the common and station-specific terms without altering the total timing error. Separate estimation therefore requires a reference constraint or gauge convention, such as a prescribed network reference together with appropriately constrained station and channel residuals. In the present forward analysis, Eq. (8) is used primarily to identify timing modes to which particular measurements are invariant or sensitive.

This spatial and channel taxonomy is summarised in Fig. 1. Absolute-time measurements can retain sensitivity to all components of Eq. (8), whereas differential measurements suppress particular timing modes. For corresponding channels at stations i and j, cancellation of a constant network-wide contribution gives

$$\Delta\delta t_{ij,c} = \left(\delta t_i - \delta t_j\right) + \left(\delta t_{ic}^{\mathrm{ch}} - \delta t_{jc}^{\mathrm{ch}}\right). \qquad (9)$$

If channel-dependent residual delays are negligible or have already been corrected, Eq. (9) reduces to $\Delta\delta t_{ij} = \delta t_i - \delta t_j$. Similarly, when all three components of one station share the same effective clock and digital latency, a common translation preserves their intrinsic relative timing and therefore does not intrinsically rotate their zero-lag polarisation covariance, apart from finite-window selection effects in non-stationary waveforms. Cancellation of common timing error is exact only for a contribution that is effectively constant over the temporal separation relevant to the observable. If a common timing process varies with time, observations occurring at reference epochs $t_{\mathrm{r},i}$and $t_{\mathrm{r},j}$ retain the residual

$$\Delta\delta t_{ij}^{\mathrm{net}} = \delta t_{\mathrm{net}}\left(t_{\mathrm{r},i}\right) - \delta t_{\mathrm{net}}\left(t_{\mathrm{r},j}\right), \qquad (10)$$

which need not vanish. Thus, *common mode* and *irrelevant to differential measurements* are not equivalent concepts. A constant common offset cancels under differencing, whereas a common fractional-frequency error, drift, or other time-varying process can re-enter through the finite temporal separation between observations. The same principle applies to three-component measurements when an identical time warp varies appreciably within a finite non-stationary analysis window.

Spatial topology must therefore be complemented by the temporal structure of the clock process. A useful phenomenological representation is

$$\delta t(t) = b + \int_{t_0}^{t} y_{\mathrm{s}}(\tau)\,\mathrm{d}\tau + r(t) + J(t), \qquad (11)$$

https://doi.org/10.5194/egusphere-2026-5154
Preprint. Discussion started: 2 November 2026
© Author(s) 2026. CC BY 4.0 License.

where b is a constant timing-offset term, distinct from the ensemble-mean timing error b_t defined in Eq. (2), $y_s(t)$ is a smooth or slowly varying component of fractional-frequency error, $r(t)$ represents residual stochastic time fluctuations not included in that smooth component, and $J(t)$ describes discrete timing discontinuities. When required, the latter may be represented as $J(t) = \sum_k A_k\, H(t - t_k)$, where A_k and t_k are the amplitude and occurrence time of the k-th jump and H is the Heaviside function.
For sufficiently regular realisations and away from jumps, the total fractional-frequency error is

$$y(t) = \frac{\mathrm{d}\delta t(t)}{\mathrm{d}t} = y_s(t) + \frac{\mathrm{d}r(t)}{\mathrm{d}t}. \qquad (12)$$

This decomposition avoids double counting between smooth frequency evolution and residual stochastic fluctuations. A constant y_s produces approximately linear growth of timing error, whereas systematic temporal evolution of y_s produces nonlinear drift. The stochastic term $r(t)$ introduces fluctuations whose statistical properties depend on the underlying oscillator-noise process and the timescale considered. For stochastic processes for which a pointwise derivative is not defined, fractional-frequency stability is characterised through finite-time frequency averages rather than through Eq. (12).
The temporal taxonomy is illustrated in Fig. 2. A static offset translates the time axis. A fractional-frequency error accumulates progressively and can produce substantial timing offsets over sufficiently long deployments. Smooth nonlinear drift produces curvature in the timing-error trajectory, stochastic oscillator processes introduce scale-dependent fluctuations, and discrete jumps produce piecewise discontinuities that cannot generally be represented by a single drift rate. These distinctions are standard in time-and-frequency metrology (Allan, 1966; Barnes et al., 1971; Riley, 2008) and are particularly relevant to autonomous deployments, for which small fractional-frequency errors may accumulate into appreciable absolute timing offsets during long holdover intervals.
The temporal model also determines whether a timing perturbation can be represented by a single delay within an analysis window. For a sufficiently smooth clock process over a short window centred at t_c, the timing error can be represented locally as $\delta t(t) \simeq \delta t(t_c) + y(t_c)(t - t_c)$, up to higher-order temporal variation. If the accumulated change $| y(t_c) | T_w$ is negligible for the measurement under consideration, a local constant-delay approximation can be adequate. Otherwise, the fractional-frequency term produces a resolvable time warp across the window, and curvature or faster temporal variability may require higher-order representation. The controlled experiments used later employ finite static perturbations when the objective is to isolate instantaneous measurement sensitivity, while Eqs. (11)–(12) retain the longer-term processes required to interpret clock stability and deployment-scale timing performance.
For a distributed acquisition system, the joint timing state can be represented by

$$\boldsymbol{\delta t}(t) = [\delta t_1(t) \quad \delta t_2(t) \quad \cdots \quad \delta t_M(t)]^{\mathrm{T}}, \qquad (13)$$

where the M timing degrees of freedom may correspond, depending on the measurement, to stations, individual channels, acquisition nodes, or another explicitly defined set of timing states. With mean vector $\boldsymbol{\mu}_t(t) = \mathbb{E}[\boldsymbol{\delta t}(t)]$, the two-time covariance is

$$\boldsymbol{\Sigma}_t(t, t') = \mathbb{E}\left[\left(\boldsymbol{\delta t}(t) - \boldsymbol{\mu}_t(t)\right)\left(\boldsymbol{\delta t}(t') - \boldsymbol{\mu}_t(t')\right)^{\mathrm{T}}\right]. \qquad (14)$$

For a measurement window over which this covariance can be treated as approximately constant, I denote the corresponding equal-time covariance by $\boldsymbol{\Sigma}_t = \boldsymbol{\Sigma}_t(t, t)$. Its diagonal elements describe marginal timing variances, whereas the off-diagonal elements quantify shared fluctuations. This distinction directly controls differential observables. For two timing states i and j,

$$\mathrm{Var}\left(\delta t_i - \delta t_j\right) = \Sigma_{t,ii} + \Sigma_{t,jj} - 2\Sigma_{t,ij}. \qquad (15)$$

For equal marginal timing standard deviations σ_t and pairwise correlation coefficient ρ,

$$\sigma_{\Delta t} = \sigma_t\sqrt{2(1 - \rho)}. \qquad (16)$$

https://doi.org/10.5194/egusphere-2026-5154
Preprint. Discussion started: 2 November 2026
© Author(s) 2026. CC BY 4.0 License.

Two systems having the same marginal timing standard deviation can therefore exhibit fundamentally different differential timing performance. Perfectly correlated fluctuations give $\sigma_{\Delta t} = 0$, whereas independent equal-variance errors give $\sigma_{\Delta t} = \sqrt{2}\sigma_t$. Consequently, a scalar station-level timing specification is insufficient for measurements whose sensitivity is controlled by pairwise or multichannel timing differences.

Spatial or inter-channel covariance must not be confused with temporal clock stability. Time-and-frequency metrology characterises oscillator stability through the fractional-frequency process $y(t)$. For averages over intervals of duration τ, the Allan deviation is

$$\sigma_y(\tau) = \left\{\frac{1}{2}\mathbb{E}\left[\left(\bar{y}_{k+1}(\tau) - \bar{y}_k(\tau)\right)^2\right]\right\}^{1/2}, \qquad (17)$$

where $\bar{y}_k(\tau)$ is the fractional-frequency error averaged over the k-th interval. Allan deviation characterises fractional-frequency stability as a function of averaging time and was introduced to overcome limitations of conventional variance for common oscillator-noise processes (Allan, 1966; Barnes et al., 1971). Complementary time-domain measures, particularly time deviation, can be used to characterise accumulated time stability (Riley, 2008).

The distinction between $\sigma_y(\tau)$ and $\mathbf{\Sigma}_t$ is fundamental. Allan deviation describes how oscillator fractional-frequency instability evolves with averaging time, whereas $\mathbf{\Sigma}_t$ describes the joint effective timing-error structure relevant to a specified seismic measurement. A favourable Allan deviation does not by itself determine the covariance of simultaneous timing errors across a network, and small instantaneous differential timing variance does not guarantee long-term clock stability during holdover. Conversely, a common reference may generate strongly correlated timing errors even when individual stations retain appreciable absolute-time error. A complete timing-performance description therefore requires both the temporal stability of the contributing clocks and the spatial or channel covariance of the effective timing errors entering the measurement.

These quantities constitute the inputs to the forward models developed in Sect. 3. Where a seismic measurement depends linearly on timing perturbations, the corresponding mean and covariance can be propagated analytically. For nonlinear observables, the complete distribution may instead be propagated numerically. Monte Carlo sampling may then represent either a physical ensemble of stochastic timing realisations or, when the input distributions encode state-of-knowledge uncertainty, an uncertainty-propagation calculation in the sense of GUM Supplement 1 (JCGM, 2008b). Maintaining this distinction between physical timing variability and uncertainty about an incompletely known timing state is essential when propagated distributions are subsequently converted into task-dependent admissibility probabilities.

3 Forward propagation into seismic measurements

The metrological quantities introduced in Sect. 2 acquire practical meaning only after they are propagated through a specific seismic measurement operator. The same residual timing perturbation can be negligible for one observable and dominant for another because spectral phase, differential delay, three-component polarisation, array slowness, backazimuth, and coherent beamforming depend on different combinations of absolute, relative, and spatially correlated timing errors. This section therefore defines the forward mappings required by the subsequent benchmarks while retaining only the mathematical relations needed to interpret task-dependent admissibility in the main text.

I adopt the Fourier-transform convention

$$X(f) = \int_{-\infty}^{+\infty} x(t)\exp(-i2\pi f t)\,\mathrm{d}t. \qquad (18)$$

For a signal affected by a constant residual timing error δt, the corresponding spectrum is

$$Y(f) = X(f)\exp(-i2\pi f\delta t), \qquad (19)$$

and the unwrapped spectral-phase error is therefore

$$\Delta\phi(f) = -2\pi f\delta t. \qquad (20)$$

https://doi.org/10.5194/egusphere-2026-5154
Preprint. Discussion started: 2 November 2026
© Author(s) 2026. CC BY 4.0 License.

This linear relation between residual timing error and frequency-dependent phase perturbation is also exploited in seismic timing-recovery methods (Weemstra et al., 2021). For an admissible unwrapped phase-error magnitude $\phi_{\max} > 0$ and $f > 0$,

$$| \delta t | \leq \frac{\phi_{\max}}{2\pi f}. \qquad (21)$$

Thus, the deterministic timing tolerance associated with a fixed phase criterion decreases inversely with frequency. Phase is treated as unwrapped because a delay corresponding to an integer multiple of 2π at one frequency is not physically equivalent to zero timing error across a broadband seismic signal. Equations (18)–(21) define the deterministic single-path phase benchmark used in Fig. 3.

For a zero-mean Gaussian residual timing error with standard deviation σ_t, the probability of satisfying the same phase criterion is

$$P\left(| \Delta\phi | \leq \phi_{\max}\right) = 2\Phi\left(\frac{\phi_{\max}}{2\pi f \sigma_t}\right) - 1, \qquad (22)$$

where Φ denotes the standard normal cumulative distribution function. For a required success probability p_0, the corresponding admissible single-path timing standard deviation is

$$\sigma_{t,\max}^{(\phi)} = \frac{\phi_{\max}}{2\pi f \, z_{(1+p_0)/2}}, \qquad (23)$$

where $z_q = \Phi^{-1}(q)$. Even for the single task of spectral-phase preservation, admissibility therefore depends jointly on frequency, the selected phase tolerance, and the probability required to satisfy it.

Differential measurements depend instead on differences between timing states. For two stations, channels, or acquisition nodes with residual timing errors δt_i and δt_j, the timing contribution to the measured differential delay is

$$\Delta\tau_{ij}^{\mathrm{err}} = \delta t_i - \delta t_j. \qquad (24)$$

Its variance and standard deviation follow directly from Eqs. (15)–(16). For a zero-mean Gaussian differential timing error with $\sigma_{\Delta t} > 0$, the probability of remaining within an admissible delay error $\tau_{\max}$ is

$$P\left(| \Delta\tau_{ij}^{\mathrm{err}} | \leq \tau_{\max}\right) = 2\Phi\left(\frac{\tau_{\max}}{\sigma_{\Delta t}}\right) - 1. \qquad (25)$$

For equal marginal timing standard deviations σ_t, pairwise correlation coefficient $\rho < 1$, and required probability p_0, Eq. (16) gives

$$\sigma_{t,\max}^{(\Delta\tau)} = \frac{\tau_{\max}}{z_{(1+p_0)/2}\sqrt{2(1-\rho)}}. \qquad (26)$$

For $\rho < 1$, Eq. (26) gives the finite marginal timing standard deviation compatible with the prescribed differential-delay criterion. Independent equal-variance errors incur the familiar $\sqrt{2}$ differential penalty, whereas progressively common-mode errors increase the admissible marginal timing scale. In the limiting case $\rho = 1$, Eq. (16) gives $\sigma_{\Delta t} = 0$, so a purely differential-delay criterion provides no finite upper bound on the marginal common-mode timing standard deviation. Figure 3 deliberately juxtaposes this pairwise differential topology with the single-path spectral-phase topology of Eqs. (20)–(23); the corresponding timing scales are not the same random variable even when expressed in identical physical units.

Three-component polarisation introduces another error topology because the relevant perturbation is relative timing among nominally synchronous channels. Covariance- and eigenvector-based polarisation analyses are well established for three-component seismic records (Vidale, 1986; Jurkevics, 1988). Let the synchronised

https://doi.org/10.5194/egusphere-2026-5154
Preprint. Discussion started: 2 November 2026
© Author(s) 2026. CC BY 4.0 License.

waveform be represented by the three-component vector $\mathbf{x}(t) = [x_N(t), x_E(t), x_Z(t)]^{\mathrm{T}}$. Component-dependent timing perturbations produce

$$\tilde{\mathbf{x}}(t) = \begin{bmatrix} x_N(t - \delta t_N) \\ x_E(t - \delta t_E) \\ x_Z(t - \delta t_Z) \end{bmatrix}. \qquad (27)$$

For an analysis window $[t_a, t_a + T_w]$, the centred covariance matrix is

$$\tilde{\mathbf{C}} = \frac{1}{T_w} \int_{t_a}^{t_a+T_w} [\tilde{\mathbf{x}}(t) - \bar{\tilde{\mathbf{x}}}]\,[\tilde{\mathbf{x}}(t) - \bar{\tilde{\mathbf{x}}}]^{\mathrm{T}}\, \mathrm{d}t, \qquad (28)$$

where the overbar denotes the component-wise mean over the same analysis window. Let the ordered eigenvalues be $\tilde{\lambda}_1 \geq \tilde{\lambda}_2 \geq \tilde{\lambda}_3$, and let $\tilde{\mathbf{v}}_1$ and $\mathbf{v}_1$denote the unit-normalised principal eigenvectors of the perturbed and synchronised reference covariance matrices, respectively. Relative timing perturbations modify the cross-component covariance terms and can therefore rotate the inferred polarisation axis. I quantify the three-dimensional principal-axis error as

$$\alpha = \arccos\left(|\mathbf{v}_1^{\mathrm{T}} \tilde{\mathbf{v}}_1|\right), \qquad (29)$$

where the absolute inner product removes the inherent 180°ambiguity of an eigenvector axis. Rectilinearity is quantified as

$$R = 1 - \frac{\tilde{\lambda}_2 + \tilde{\lambda}_3}{2\tilde{\lambda}_1}. \qquad (30)$$

A timing translation common to all three components, $\delta t_N = \delta t_E = \delta t_Z$, preserves intrinsic intercomponent timing and therefore leaves the ideal zero-lag covariance unchanged when the analysis window is translated consistently. In a finite non-stationary window, selection effects can nevertheless produce an indirect change, as examined in the supplementary robustness analysis. By contrast, a relative intercomponent delay produces a phase difference obtained directly by applying Eq. (20) to the difference between channel timing errors. Because the perturbed channels enter Eq. (28) before eigendecomposition, the resulting angular error can be nonlinear and non-monotonic with timing skew, motivating the direct numerical treatment in Fig. 4.
For a prescribed principal-axis tolerance $\alpha_{\max}$, let the connected admissible interval containing zero relative delay be

$$\mathcal{I}_0 = \{\delta : \alpha(\delta) < \alpha_{\max}\}_0, \qquad (31)$$

where the subscript 0 denotes the connected component containing $\delta = 0$. A conservative symmetric radius of that interval is

$$\delta t^\star = \inf\{|\,\delta\,| > 0 : \alpha(\delta) \geq \alpha_{\max}\}. \qquad (32)$$

If the relative intercomponent delay is represented by a zero-mean Gaussian variable with standard deviation σ_{rel}, a sufficient two-sided admissibility bound is

$$\sigma_{\mathrm{rel,max}}^{(\mathrm{pol})} = \frac{\delta t^\star}{z_{(1+p_0)/2}}. \qquad (33)$$

Here, σ_{rel} refers specifically to the standard deviation of the relative intercomponent delay, not to the marginal timing uncertainty of an individual channel. For two independent channels having equal marginal timing standard deviation σ_{ch}, for example, $\sigma_{\mathrm{rel}} = \sqrt{2}\sigma_{\mathrm{ch}}$. This distinction is essential because polarisation

https://doi.org/10.5194/egusphere-2026-5154
Preprint. Discussion started: 2 November 2026
© Author(s) 2026. CC BY 4.0 License.

admissibility cannot generally be represented by the same scalar timing quantity used for independent station errors.

Array measurements introduce a spatial projection problem. For M stations in a planar array, the arrival-time vector is represented as

$$\mathbf{t} = t_0\mathbf{1} + \mathbf{G}\mathbf{p} + \boldsymbol{\delta t}, \qquad (34)$$

where t_0 is an intercept, $\mathbf{G}$ contains the station east and north coordinates, $\mathbf{p}$ is the horizontal propagation-slowness vector, and $\boldsymbol{\delta t}$ is the residual station timing-error vector. This is the plane-wave geometry underlying conventional array and frequency–wavenumber analysis (Capon, 1969; Rost and Thomas, 2002).

For a full-rank receiver geometry centred with respect to the adopted weighting, the timing-induced slowness perturbation can be written as

$$\boldsymbol{\Delta p} = \mathbf{H}\boldsymbol{\delta t}, \qquad \mathbf{H} = \left(\mathbf{G}^{\mathrm{T}}\mathbf{W}\mathbf{G}\right)^{-1}\mathbf{G}^{\mathrm{T}}\mathbf{W}, \qquad (35)$$

where $\mathbf{W}$ is the weighting matrix. The complete weighted least-squares derivation, including the fitted intercept and centring condition, is given in Appendix A. An array-common constant timing offset is absorbed by t_0 and therefore does not perturb $\mathbf{p}$. In contrast, for a spatially linear timing field of the form $\boldsymbol{\delta t} = b\mathbf{1} + \mathbf{G}\mathbf{g}$, Eq. (35) gives

$$\boldsymbol{\Delta p} = \mathbf{g}. \qquad (36)$$

A linear spatial timing gradient is therefore algebraically indistinguishable from an equivalent slowness perturbation under the stated full-rank plane-wave model. This exact degeneracy motivates the timing–geometry–propagation confounding analysis presented in the Supplement.

The backazimuth convention adopted throughout is

$$\mathbf{p} = -u\begin{bmatrix}\sin\theta\\ \cos\theta\end{bmatrix}, \quad u = \| \mathbf{p} \|, \quad v_{\mathrm{app}} = \frac{1}{u}, \qquad (37)$$

where θ is measured clockwise from North towards the source, $u$is horizontal slowness magnitude, and v_{app} is apparent horizontal velocity. If the residual timing-error vector has covariance $\boldsymbol{\Sigma}_t$, its contribution to slowness covariance is

$$\boldsymbol{\Sigma}_p = \mathbf{H}\boldsymbol{\Sigma}_t\mathbf{H}^{\mathrm{T}}. \qquad (38)$$

The corresponding mean perturbation is $\mathbb{E}[\boldsymbol{\Delta p}] = \mathbf{H}\boldsymbol{\mu}_t$. Thus, deterministic or mean timing structure displaces the inferred slowness, whereas stochastic timing covariance produces a geometry-dependent uncertainty region. Poorly conditioned arrays amplify timing errors preferentially along weakly constrained directions. The independent equal-variance special case and the complete weighted least-squares propagation are retained in Appendix A. Figure 5 evaluates the resulting backazimuth and apparent-velocity sensitivity; the backazimuth probability is computed without linearising the angular transformation.

Coherent beamforming depends principally on residual interstation phase differences. For a zero-mean multivariate Gaussian station timing-error vector with covariance Σ_t, the expected timing-induced off-diagonal pairwise phase-coherence retention is

$$C_B(f) = \frac{1}{M(M-1)}\sum_{i\neq j}\exp\left[-2\pi^2 f^2\left(\Sigma_{t,ii} + \Sigma_{t,jj} - 2\Sigma_{t,ij}\right)\right]. \qquad (39)$$

Let $B(f)$ denote the normalised, correctly steered timing-only beam defined explicitly in Appendix B. Under the equal-amplitude, equal-weight benchmark, its expected normalised coherent power is

$$\mathbb{E}\left[|\, B(f)\,|^2\right] = \frac{1}{M} + \left(1 - \frac{1}{M}\right) C_B(f). \qquad (40)$$

https://doi.org/10.5194/egusphere-2026-5154
Preprint. Discussion started: 2 November 2026
© Author(s) 2026. CC BY 4.0 License.

The first term is diagonal self-power and does not represent interstation coherence. Consequently, $C_B(f)$ isolates the expected retention of pairwise phase coherence: independent timing errors, partially common timing errors, spatially correlated timing errors, and perfectly common-mode timing errors can have identical marginal variance while yielding markedly different coherence. The Gaussian characteristic-function derivation and the independent, equicorrelated, and perfectly common-mode special cases are given in Appendix B. The spatial covariance models used for the numerical benchmark are specified separately in Sect. 4 rather than embedded in the general theory.

The preceding operators motivate a common definition of task-dependent timing admissibility. Let k denote a seismic measurement task and $\mathcal{E}_k$ its associated error or degradation metric. In the general case,

$$\mathcal{E}_k = \mathcal{F}_k(f, \boldsymbol{\mu}_t, \boldsymbol{\Sigma}_t, \mathcal{D}_t, \mathcal{T}_t, \mathbf{G}, \mathbf{p}, \mathrm{SNR}, T_w, \mathcal{W}, \dots), \qquad (41)$$

where $\mathcal{D}_t$ denotes the timing-error distributional family, $\mathcal{T}_t$ denotes its topology or sharing structure, SNR denotes the Signal-to-Noise Ratio and $\mathcal{W}$ collects additional wavefield and processing properties relevant to the task. For particular cases, this general description reduces to a smaller parameter set determined by the selected timing model and measurement operator.

For deterministic timing states, admissibility is assessed directly against a task-specific tolerance ϵ_k. For stochastic timing errors or uncertain timing states, the corresponding requirement is

$$P(\mathcal{E}_k \le \epsilon_k) \ge p_0. \qquad (42)$$

Because some measurement errors, notably narrow-band polarisation metrics, need not vary monotonically with timing-error magnitude, a scalar admissible timing scale must not be defined merely from an arbitrary distant threshold crossing. Consider a one-parameter timing-model family indexed by a non-negative scale s, with all other properties held fixed. I define the admissible scale as the largest interval connected to the zero-error state:

$$s_{\max}^{(k)} = \sup\{s \ge 0 : P_\xi(\mathcal{E}_k \le \epsilon_k) \ge p_0 \quad \text{for all } 0 \le \xi \le s\}, \qquad (43)$$

where P_ξ denotes the probability measure associated with the timing-error model having scale ξ. For a monotonic Gaussian station-error family, s may simply be σ_t; for relative intercomponent timing, σ_{rel} is the appropriate native scale. The connected-from-zero definition prevents non-monotonic re-entry at larger timing errors from generating an artificial admissibility limit.

The central implication is that timing admissibility is conditional on the measurement task, frequency content, timing-error topology and distribution, timing covariance, receiver geometry, wavefield properties, signal-to-noise ratio, and analysis procedure rather than being reducible to a universal inequality of the form $\sigma_t <$ constant. Relative intercomponent timing uncertainty, independent station timing uncertainty, common-mode timing uncertainty, and spatial timing gradients therefore remain distinct error structures even when their nominal magnitudes share the same physical unit. Figures 3–6 provide controlled realisations of these forward operators for spectral phase, differential delay, polarisation, array parameter estimation, and coherent beamforming; Sect. 4 describes the synthetic, observational, and public-array benchmarks used to evaluate their task-specific consequences.

4 Data and methods

The numerical experiments were designed to quantify the forward consequences of residual timing errors for the measurement operators defined in Sect. 3 rather than to infer a universal timing requirement for a seismic acquisition system. Timing perturbations were therefore imposed on otherwise identical synthetic or observational waveforms, with their topology, distribution, covariance, and amplitude controlled explicitly. Deterministic timing offsets and gradients were treated separately from zero-mean stochastic residuals, and all probabilistic thresholds were evaluated in the native timing-error variable of the corresponding task.

The spectral-phase and differential-delay experiments shown in Fig. 3 implement the single-path and pairwise formulations of Eqs. (20)–(26). Deterministic single-path offsets of 1, 10, and 100 ms were propagated over frequency using the Fourier timing operator of Eq. (19). Maximum deterministic offsets were evaluated for

https://doi.org/10.5194/egusphere-2026-5154
Preprint. Discussion started: 2 November 2026
© Author(s) 2026. CC BY 4.0 License.

illustrative unwrapped phase tolerances of 5°, 15°, and 30°. The corresponding stochastic single-path experiment assumed zero-mean Gaussian residual timing errors and evaluated the probability in Eq. (22), with the 15°criterion displayed explicitly in the frequency–timing probability map. Differential timing was evaluated independently using Eqs. (15), (16), (24), and (25). Two timing states were assigned equal marginal standard deviation $\sigma_t$and variable correlation coefficient ρ, including anti-correlated, independent, partially common-mode, and perfectly common-mode limits. Differential-delay admissibility used an illustrative absolute tolerance of 10 ms and a required probability of 0.95. All tolerances in Fig. 3 are controlled benchmark choices used to expose the dependence of timing admissibility on frequency and covariance rather than proposed instrument specifications.

The propagation of intercomponent timing inconsistency into three-component polarisation was evaluated using the covariance-eigenvector operator of Eqs. (27)–(33). The main controlled wavefield was linearly polarised, noise free, and narrow band, with reference horizontal azimuth 40°and incidence angle 35°. Only the east component was delayed; the north and vertical components retained the reference time base. Deterministic E-component timing skew ranged from 0 to 25 ms, while signal amplitude and waveform shape were otherwise held fixed. The benchmark frequencies were 1, 5, 10, and 20 Hz. The principal polarisation axis, polarisation azimuth, incidence angle, and rectilinearity were obtained from the centred covariance matrix and its eigensystem. The 180°principal-axis ambiguity was resolved relative to the synchronised synthetic reference direction.

The deterministic polarisation experiment was complemented by zero-mean Gaussian relative E-versus-N/Z timing errors. For each frequency and wavefield orientation, the first deterministic crossing of the prescribed principal-axis tolerance defined the connected-from-zero admissible interval according to Eqs. (31)–(32), and Eq. (33) was then used to obtain the corresponding 95 % timing-only admissibility scale. The main polarisation benchmark used an illustrative 5° principal-axis tolerance. Sensitivity to incidence angle was evaluated at 20°, 45°, and 70°while retaining a fixed azimuth of 40°. No additive noise, response mismatch, component-orientation error, or propagation error was introduced in this controlled experiment.

Array-direction sensitivity was evaluated using the plane-wave model and timing-to-slowness projection of Eqs. (34)–(38) and Appendix A. Three 15-station geometries were considered: approximately isotropic, elongated, and irregular receiver distributions, each scaled to an Root-Mean-Square (RMS) radius of 10 km. Equal station weights were used throughout this controlled array benchmark. The controlled incident wavefield had horizontal slowness $u = 0.08$ s km^{-1}and backazimuth 40°. Deterministic spatial timing gradients were used to verify the exact timing-gradient/slowness degeneracy of Eq. (36), while stochastic backazimuth uncertainty was evaluated by adding independent zero-mean Gaussian station timing errors to the synthetic arrival times and recovering the apparent slowness using the same plane-wave model.

Backazimuth (BAZ) error was defined through the minimum circular angular distance between the perturbed and reference directions. The principal probabilistic benchmark required $P(|\,\Delta\mathrm{BAZ}\,| \leq 5^\circ) \geq 0.95$, with the probability evaluated without linearising the angular transformation. For each geometry, the maximum admissible independent station timing standard deviation was determined according to the connected-from-zero definition of Eq. (43). Gaussian angular probabilities were evaluated deterministically using 80-node Gauss–Hermite quadrature rather than finite Monte Carlo sampling. Additional robustness calculations varied array radius, station count, and source backazimuth, with the extended geometry sensitivity reported in the Supplement. Phase identification and association were assumed to remain fixed and correct throughout, so the experiment isolates post-association parameter-estimation sensitivity.

The independent-station-error benchmark was then generalised to structured timing covariance for the beam-coherence calculations in Fig. 6. Four zero-mean Gaussian covariance models were evaluated. Independent station timing errors were represented by

$$\boldsymbol{\Sigma}_t^{(\mathrm{ind})} = \sigma_t^2 \mathbf{I}. \qquad (44a)$$

An equicorrelated timing model was represented by

$$\boldsymbol{\Sigma}_t^{(\mathrm{eq})} = \sigma_t^2[(1-\rho)\mathbf{I} + \rho\,\mathbf{1}\mathbf{1}^{\mathrm{T}}]. \qquad (44b)$$

Spatially correlated timing errors were represented using an exponential covariance kernel,

https://doi.org/10.5194/egusphere-2026-5154
Preprint. Discussion started: 2 November 2026
© Author(s) 2026. CC BY 4.0 License.

$$\Sigma_{t,ij}^{(\mathrm{sp})} = \sigma_t^2 \exp\left(-\frac{d_{ij}}{L_c}\right), \qquad (44c)$$

where d_{ij} is the distance between stations $i$and j, and L_c is the spatial timing-correlation length. Finally, the limiting perfectly common-mode model was represented by

$$\boldsymbol{\Sigma}_t^{(\mathrm{cm})} = \sigma_t^2 \mathbf{1}\mathbf{1}^{\mathrm{T}}. \qquad (44d)$$

For the M-station equicorrelated model, positive semidefiniteness requires $-1/(M-1) \le \rho \le 1$; the numerical benchmarks considered here use non-negative correlation. All four models have the same station-wise marginal variance σ_t^2 and differ in their covariance topology.

The reference covariance calculations used 15-station arrays with 10 km RMS radius, $\rho = 0.8$ for the representative equicorrelated model, $L_c = 10$ km for the representative spatially correlated model, $\sigma_t = 10$ ms, and $f = 10$ Hz where a single reference frequency was required. Isotropic, elongated, and irregular arrays having the same RMS radius were used to isolate the effect of the station-separation distribution under spatially correlated timing errors. Timing-induced pairwise phase-coherence retention and expected normalised beam power were calculated from Eqs. (39)–(40). An illustrative criterion $C_B = 0.90$ was used to define coherence-based timing limits.

The analytical Gaussian expectations were independently verified for selected covariance configurations using 30 000 Monte Carlo realisations. Each realisation sampled the multivariate timing-error distribution specified by Eq. (44), after which pairwise timing-induced phase factors were evaluated directly. The Monte Carlo estimator excluded diagonal self-power terms and therefore targeted the same off-diagonal quantity C_B defined in Eq. (39). Equal signal amplitudes, correct beam steering, Gaussian residual timing errors, and the absence of additive waveform noise, response mismatch, phase-identification error, and propagation-model error were intentional assumptions of this controlled benchmark.

The analytical and synthetic experiments were followed by an observational waveform perturbation benchmark based on the public three-component RJOB example distributed with ObsPy. The benchmark uses the north, east, and vertical components of the example record (EHN, EHE, and EHZ), all sampled at 200 Hz. ObsPy provides the open-source waveform and processing environment used for this experiment (Beyreuther et al., 2010; Megies et al., 2011; Krischer et al., 2015). For deterministic reproduction, the associated figure package contains the raw waveform segment spanning 25.00–32.17 s relative to the origin of the public example record. The documented ObsPy autoregressive-picker example gives temporal markers $t_P = 30.635$ s and $t_S = 31.280$ s. These values were used only as reproducible processing references and were not treated as independently validated phase determinations. Each component was linearly detrended and processed using a fourth-order Butterworth band-pass filter applied forward and backward through second-order sections, producing a zero-phase response. Three analysis bands were considered: 4–8, 8–12, and 12–16 Hz. Artificial timing perturbations were applied after band-pass filtering and before extraction of the polarisation window. The central analysis interval was 30.60–31.25 s and therefore terminated before the documented S marker. Because forward–backward filtering is acausal, this interval is described as a P-arrival-centred, pre-S analysis window of the filtered observational waveform rather than as an uncontaminated isolated P-wave segment.

Filter-edge behaviour was checked explicitly. The radii containing 99.9 % of the energy of the corresponding two-sided zero-phase impulse responses were approximately 0.685, 0.645, and 0.630 s for the 4–8, 8–12, and 12–16 Hz filters, respectively. Each value is smaller than the minimum 0.92 s data margin available around the analysis windows within the retained waveform segment. The central processing configuration used a Tukey taper with $\alpha = 0.15$. Processing sensitivity was evaluated using six entirely pre-S windows—30.55–31.20, 30.55–31.25, 30.60–31.20, 30.60–31.25, 30.65–31.20, and 30.65–31.25 s—crossed with $\alpha = 0.05$, 0.15, and 0.25, yielding 18 predefined configurations.

Artificial timing perturbations were applied only to EHE, with EHN and EHZ retained as synchronised references. Relative E-channel delays ranged from 0 to 20 ms and were implemented as fractional-sample delays through the Fourier timing operator of Eq. (19), using 2 s of reflection padding before transformation to suppress circular wrap-around artefacts. This implementation permits continuously varying timing perturbations below the 5 ms sampling interval of the 200 Hz waveform. For every frequency band, imposed delay, analysis window, and taper, the selected samples were demeaned and tapered before computation of the polarisation covariance. The covariance estimator was normalised by the sum of squared taper weights, and

https://doi.org/10.5194/egusphere-2026-5154
Preprint. Discussion started: 2 November 2026
© Author(s) 2026. CC BY 4.0 License.

principal-axis orientation was recovered using the same eigensystem definition as in the controlled polarisation experiment. Perturbed eigenvector polarity was aligned independently to the corresponding synchronised reference eigenvector.

Instrument responses were not removed from the RJOB example. Any fixed response, orientation, site, and waveform characteristics are therefore shared by the synchronised and perturbed cases and are not interpreted as timing effects. The experiment consequently measures reference-relative sensitivity to controlled intercomponent timing perturbations rather than providing an absolute estimate of source polarisation or a statistically representative earthquake-waveform sample.

The final benchmark transferred the framework to a public real-array geometry while retaining controlled wavefield and timing perturbations. I used the five-station AGFA geometry distributed with the official ObsPy frequency–wavenumber analysis example. The station coordinates used in the calculations were 48.108589°N, 11.582967°E; 48.108192°N, 11.583120°E; 48.108692°N, 11.583414°E; 48.108456°N, 11.583049°E; and 48.108730°N, 11.583157°E. Their centroid is 48.1085318°N, 11.5831414°E, and the corresponding RMS array radius is approximately 0.02437 km. The broader AGFA experimental context has been documented by Wassermann et al. (2009) and Maranò and Fäh (2014), whereas the exact five-station subset follows the public ObsPy example. No AGFA waveform data were analysed.

The controlled AGFA reference wavefield used backazimuth 270°and horizontal slowness $u = 1.5\ \mathrm{s\,km^{-1}}$. For the beam experiment in Fig. 8b, a spatially linear timing gradient of $0.20\ \mathrm{s\,km^{-1}}$, oriented 60°clockwise from North, was imposed across the five stations. For this compact geometry, the imposed field corresponds to approximately 3.37 ms RMS and 9.34 ms peak-to-peak station timing variation. Broadband beam power was evaluated over candidate horizontal slowness vectors by coherently summing frequency-dependent station phase factors and integrating the squared beam amplitude using the empirical spectral weighting defined below. Agreement between the analytically shifted slowness and the numerically recovered beam maximum is used as an internal consistency test of the controlled full-rank plane-wave model rather than as independent observational validation.

The empirical spectral weighting used in Figs. 8b and 8d was derived from the public RJOB EHZ waveform. The embedded EHZ segment was linearly detrended and filtered between 4 and 8 Hz using the same fourth-order zero-phase Butterworth implementation. The interval 30.30–31.20 s was extracted, demeaned, and tapered using a Tukey window with $\alpha = 0.20$. A one-sided spectrum was calculated using a real Fourier transform with $N_{\mathrm{FFT}} = 4096$, and only samples within 4–8 Hz were retained. The normalised empirical spectral weights were

$$w_k = \frac{|\,W(f_k)\,|^2}{\sum_{m:\,4\le f_m\le 8\ \mathrm{Hz}} |\,W(f_m)\,|^2},\quad 4 \le f_k \le 8\ \mathrm{Hz}, \qquad (45)$$

where $W(f_k)$ denotes the complex coefficient of the retained one-sided Fourier spectrum at frequency f_k. These weights characterise only the selected RJOB EHZ interval; no AGFA waveform information enters the spectral weighting.

Directional timing admissibility for the AGFA geometry was calculated by propagating independent zero-mean Gaussian station timing errors through Eqs. (34)–(38) and evaluating the exact backazimuth criterion used for Fig. 5. The reference configuration used BAZ = 270°and $u = 1.5\ \mathrm{s\,km^{-1}}$, while the broader controlled sensitivity calculation varied both true backazimuth and horizontal slowness. The same 5°, 95 % criterion was retained. Phase identification and association were again assumed fixed and correct, so Fig. 8c represents post-association directional parameter sensitivity rather than detection or phase-association performance.

Figure 8d addresses a distinct, geometry-independent error topology. For independent zero-mean Gaussian station timing errors having common marginal standard deviation σ_t, Eq. (15) gives pairwise timing-difference variance $2\sigma_t^2$. Combining this result with Eq. (39) and the empirical spectral weights of Eq. (45) gives the RJOB-weighted broadband pairwise phase-coherence retention

$$\bar{C}_B\,(\sigma_t) = \sum_k w_k \exp\!\left(-4\pi^2 f_k^2 \sigma_t^2\right). \qquad (46)$$

The sum in Eq. (46) extends over the retained 4–8 Hz Fourier samples defined in Eq. (45). This analytical broadband expectation was independently verified using 5000 Monte Carlo realisations at each selected

https://doi.org/10.5194/egusphere-2026-5154
Preprint. Discussion started: 2 November 2026
© Author(s) 2026. CC BY 4.0 License.

timing-uncertainty level. As in the monochromatic coherence benchmark, the Monte Carlo estimator excluded diagonal self-power contributions and therefore targeted pairwise timing coherence rather than total finite-array power.

The remaining synthesis calculations in Fig. 8 compare task-specific admissibility scales while retaining their native timing-error topologies. The spectral-phase criterion uses a zero-mean Gaussian single-path residual timing error with a 15°, 95 % phase criterion according to Eq. (23). The polarisation criterion uses the standard deviation of E-channel timing relative to synchronised N/Z, with a 5°, 95 % principal-axis criterion evaluated for the 45°-incidence, 40°-azimuth member of the controlled Fig. 4 family rather than the 35°main reference configuration. The array criterion uses independent station timing errors and the 5°, 95 % backazimuth condition for the marked AGFA configuration. The beam criterion uses independent station timing errors and the monochromatic expected pairwise-coherence condition $C_B \geq 0.90$. These scales are displayed together because they share the physical unit of time, but they are not treated as estimates of a common timing-error random variable or collapsed into a universal minimum requirement.

The numerical experiments deliberately distinguish deterministic forward propagation, analytical stochastic propagation, and simulation-based verification. Figure 3 combines deterministic spectral-phase propagation with Gaussian single-path and differential-delay probabilities; Fig. 5 uses deterministic Gauss–Hermite quadrature for Gaussian backazimuth probabilities; Fig. 6 evaluates analytical multivariate-Gaussian coherence and verifies selected cases by Monte Carlo simulation; and Fig. 8d independently verifies the broadband analytical expectation against Monte Carlo realisations.

Supplementary Figs. S1–S6 retain the robustness and sensitivity analyses associated with the principal benchmarks. Figure S1 examines distributional robustness; Fig. S2 tests the fractional-delay and sampling implementation; Fig. S3 evaluates array-geometry robustness; Fig. S4 examines common versus differential timing perturbations; Fig. S5 assesses observational processing sensitivity; and Fig. S6 addresses identifiability among timing, receiver-position, and propagation-related perturbations. These figures remain Supplementary Material and are not part of Appendices A–B.

All waveform handling and numerical analyses were implemented in Python, using ObsPy for seismological waveform support (Beyreuther et al., 2010; Megies et al., 2011; Krischer et al., 2015) together with standard numerical routines for Fourier analysis, digital filtering, linear algebra, Gaussian quadrature, covariance propagation, and Monte Carlo verification. Public waveform segments and receiver coordinates were retained with explicit provenance, and machine-readable numerical products underlying Figs. 3–8 were generated from the same computational implementations used to construct the corresponding figures.

The experiments should therefore be interpreted as a hierarchy of controlled forward-propagation benchmarks rather than as estimates of the empirical distribution of synchronisation errors in operational seismic networks. Source complexity, site effects, instrument-response uncertainty, non-stationary waveform noise, phase-identification failure, association error, propagation-model error, and specific clock-failure mechanisms are excluded unless explicitly represented in an experiment. These restrictions deliberately isolate timing propagation, but they also imply that all reported admissibility boundaries remain conditional on the selected observable, timing-error topology, wavefield, receiver geometry, uncertainty model, processing configuration, and performance criterion.

5 Results

The forward calculations show that the effect of timing error changes markedly with both signal frequency and measurement topology. For deterministic single-path timing offsets, the magnitude of the unwrapped spectral-phase error increases linearly with the product $f\delta t$ (Fig. 3a). At 10 Hz, offsets of 1, 10, and 100 ms correspond to phase-error magnitudes of 3.6°, 36°, and 360°, respectively. The deterministic phase-tolerance curves in Fig. 3b therefore give maximum timing offsets of approximately 1.39, 4.17, and 8.33 ms at 10 Hz for illustrative phase tolerances of 5°, 15°, and 30°, respectively. Each limit decreases inversely with frequency, as predicted by Eq. (21).

The probabilistic single-path phase benchmark retains this inverse frequency scaling but applies it to a zero-mean Gaussian residual timing error rather than to a fixed deterministic offset. For the illustrative 15°, 95 % criterion shown explicitly in Fig. 3e, the admissible single-path timing standard deviation is approximately 2.13 ms at 10 Hz. This single-path probability depends on frequency, phase tolerance, and marginal timing standard deviation, but not on inter-station correlation. Correlation enters separately through the differential-delay topology. For the 10 ms, 95 % differential-delay criterion in Fig. 3d–f, the maximum equal marginal

https://doi.org/10.5194/egusphere-2026-5154
Preprint. Discussion started: 2 November 2026
© Author(s) 2026. CC BY 4.0 License.

station timing standard deviation is approximately 3.61 ms for independent errors ($\rho = 0$), 5.10 ms for $\rho = 0.5$, and 11.41 ms for $\rho = 0.9$. Negative correlation produces the opposite behaviour, increasing differential timing uncertainty above the independent-error limit for the same marginal σ_t. For fixed marginal σ_t, the differential timing standard deviation tends to zero as ρ approaches unity; equivalently, a differential-delay criterion places progressively weaker constraints on the admissible marginal timing standard deviation. Figure 3 therefore demonstrates that single-path phase admissibility and pairwise differential-delay admissibility cannot be inferred from the same scalar timing specification even when both are expressed in milliseconds.

The controlled three-component experiment shows that timing perturbations produce a distinct response when propagated into polarisation rather than into scalar spectral phase (Fig. 4). For the principal 40°-azimuth, 35°-incidence configuration, an E-only timing skew rotates the recovered principal polarisation axis and produces coupled azimuth and incidence perturbations. The angular response depends on both frequency and wavefield orientation and is not equivalent to a uniform rotation of the three-dimensional particle-motion trajectory. The incidence-angle sensitivity calculations confirm that timing response also varies with the orientation of the incident wavefield. Rectilinearity is likewise non-monotonic with relative timing skew in the narrow-band benchmark: near particular phase offsets, an apparently rectilinear trajectory can re-emerge despite an incorrect principal direction. This re-entry behaviour motivates the connected-from-zero admissibility definition rather than selection of a more distant threshold crossing.

For the 45°-incidence, 40°-azimuth sensitivity case subsequently used in the cross-task synthesis, the deterministic 5°principal-axis threshold at 10 Hz is reached at approximately 12.63 ms. Under the corresponding zero-mean Gaussian E-versus-N/Z residual timing model, the 95 % principal-axis admissibility limit is approximately 6.44 ms. The difference between the two values reflects their different deterministic and probabilistic definitions: the former identifies the first timing skew at which the deterministic angular error crosses 5°, whereas the latter constrains the standard deviation of a zero-mean relative timing distribution so that the same angular criterion is satisfied with 95 % probability.

The deterministic array calculations first confirm the exact timing-gradient/slowness degeneracy predicted by Eq. (36) (Fig. 5). For a spatial timing field lying in the column space of the receiver geometry, the recovered slowness perturbation follows the imposed timing gradient with a 1:1 relation for all three full-rank arrays, whereas an array-common constant offset is absorbed by the fitted intercept. Consequently, the deterministic gradient-induced slowness, backazimuth, and apparent-velocity biases are independent of receiver geometry under this ideal plane-wave construction.

The stochastic array experiment exhibits a different dependence because station timing perturbations are projected through receiver geometry. For the 15-station, 10 km RMS reference arrays and the 5°, 95 % backazimuth criterion, the admissible independent station timing standard deviation is approximately 97.42 ms for the isotropic geometry and 91.45 ms for the irregular geometry. These values differ despite matched station count, RMS aperture, reference slowness, and performance criterion, showing that characteristic aperture alone does not determine array timing admissibility. The timing-to-slowness projection depends on the full receiver geometry and its directional conditioning. The elongated geometry further demonstrates the anisotropy of the slowness uncertainty, while the extended aperture and station-count sensitivity analysis in Fig. S3 shows that admissible timing uncertainty generally increases as the array gains greater spatial leverage or additional receivers under the controlled assumptions.

The influence of covariance topology becomes explicit when timing performance is evaluated through inter-station phase coherence (Fig. 6). At 10 Hz and a marginal station timing standard deviation of 10 ms, independent Gaussian timing errors give an expected pairwise coherence retention of $C_B = 0.6738$. Positive equicorrelation increases the retained coherence to 0.8209 for $\rho = 0.5$, 0.9241 for $\rho = 0.8$, and 0.9613 for $\rho = 0.9$, while the perfectly common-mode limit remains $C_B = 1$ in the timing-only model. Thus, identical marginal timing variance can correspond to markedly different inter-station phase coherence solely because the off-diagonal covariance structure differs.

Spatially correlated timing errors introduce an additional geometry dependence because the differential variance of each station pair depends on its separation. For $L_c \simeq 10$ km, $\sigma_t = 10$ ms, and 10 Hz, the expected pairwise coherence is approximately 0.758 for the isotropic array, 0.775 for the elongated array, and 0.767 for the irregular array (Fig. 6). The three arrays have the same RMS radius, so these differences arise from their distinct distributions of inter-station separations relative to the correlation length. Under independent timing errors, the illustrative $C_B \geq 0.90$ criterion gives an admissible station timing standard deviation of approximately 5.17 ms at 10 Hz, with the limit decreasing approximately inversely with frequency. The analytical covariance propagation is independently reproduced by Monte Carlo calculations: across the

https://doi.org/10.5194/egusphere-2026-5154
Preprint. Discussion started: 2 November 2026
© Author(s) 2026. CC BY 4.0 License.

selected validation cases, the maximum absolute theory–simulation discrepancy in C_B is 4.29×10^{-4}. The Monte Carlo calculations also reproduce the absence of relative coherence loss for perfectly common-mode timing perturbations within the timing-only formulation.

The observational RJOB perturbation experiment shows that controlled intercomponent timing sensitivity remains measurable when the idealised particle-motion benchmark is replaced by a spectrally structured waveform (Fig. 7), although the response varies strongly among frequency bands and polarisation metrics. In the central processing configuration, the principal-axis error in the 4–8 Hz band remains comparatively small over the tested 0–20 ms E-component delay range: the errors are approximately 0.92°, 0.95°, and 0.88°at imposed delays of 5, 10, and 20 ms, respectively. The corresponding azimuth biases are approximately 3.89°, 4.19°, and −2.25°. The central-configuration response is therefore non-monotonic with imposed delay.

The 8–12 Hz band is substantially more sensitive in the same processing configuration. Principal-axis error increases from approximately 7.80°at a 5 ms E-channel delay to 26.18°at 10 ms and 68.39°at 20 ms, while the corresponding azimuth bias reaches 67.61°at 20 ms. In the 12–16 Hz band, the principal-axis errors are approximately 16.60°, 19.54°, and 22.45° at 5, 10, and 20 ms, respectively. The synchronised reference polarisation state also differs among bands, so these values quantify perturbations relative to the corresponding band-specific reference rather than deviations from a single absolute source-polarisation state.

The 18 predefined processing configurations show that the inferred angular perturbation also depends on the selected pre-S interval and taper (Fig. 7 and Fig. S5). At an imposed 10 ms E-channel delay, principal-axis errors span approximately 0.35–4.46° in the 4–8 Hz band, 20.02–45.65° in the 8–12 Hz band, and 1.61–22.34° in the 12–16 Hz band. The response therefore exhibits pronounced band dependence but not a simple monotonic ordering with nominal frequency. Millisecond-scale intercomponent timing perturbations that produce small principal-axis changes in one band can generate order-10° to several-tens-of-degrees perturbations in the two higher-frequency bands. Processing choices alter the quantitative magnitude of the response but do not support a single band-independent polarisation timing tolerance.

The compact AGFA benchmark further demonstrates the dependence of timing admissibility on receiver geometry and incident wavefield (Fig. 8). The five-station geometry has an RMS radius of approximately 0.02437 km and a two-norm geometry condition number of approximately 2.15. For the controlled BAZ = 270°, $u = 1.5$ s km^{-1}wavefield, the synchronised broadband beam maximum is recovered near the prescribed slowness coordinates, at $p_E \simeq 1.502$ s km^{-1} and $p_N = 0$. Applying the spatial timing gradient of 0.20 s km^{-1}shifts the recovered maximum to approximately $p_E = 1.672$ s km^{-1}and $p_N = 0.100$ s km^{-1}, consistently reproducing the imposed timing-gradient projection in slowness space.

For independent station timing errors, the reference AGFA configuration admits a standard deviation of approximately 2.992 ms under the 5°, 95 % backazimuth criterion (Fig. 8c). At fixed $u = 1.5$ s km^{-1}, the admissible timing standard deviation varies with source backazimuth from approximately 1.54 to 3.25 ms. Across the broader backazimuth–slowness sensitivity domain, the calculated limits range from approximately 0.51 to 5.42 ms. Directional timing admissibility therefore varies substantially within the same fixed receiver geometry as the incident slowness vector changes.

The RJOB-weighted broadband coherence calculation provides a separate timing criterion that is independent of AGFA receiver geometry (Fig. 8d). For independent station timing errors, $\bar{C}_B$ decreases from approximately 0.9953 at $\sigma_t = 2$ ms to 0.9814 at 4 ms, 0.9587 at 6 ms, 0.9279 at 8 ms, and 0.8901 at 10 ms. The $\bar{C}_B = 0.90$ crossing occurs at approximately 9.51 ms, and the retained pairwise coherence falls to approximately 0.6362 at 20 ms. A perfectly common-mode timing perturbation preserves unit pairwise coherence throughout in this timing-only formulation. The independent Monte Carlo verification reproduces the broadband analytical expectation over the tested interval, with a maximum absolute theory–simulation difference of approximately 1.96×10^{-3}.

The cross-task synthesis in Fig. 8e–f makes the non-equivalence of the native timing variables explicit. For the zero-mean Gaussian single-path spectral-phase criterion with a 15° tolerance and 95 % required probability, the admissible residual timing standard deviations at 1, 5, 10, and 20 Hz are approximately 21.26, 4.25, 2.13, and 1.06 ms, respectively. This is the probabilistic counterpart of the same 15° phase tolerance shown deterministically in Fig. 3b and probabilistically in Fig. 3e–f, rather than a separate phase criterion. For the 45°-incidence, 40°-azimuth polarisation case, the corresponding 95 % E-versus-N/Z relative timing limits are approximately 64.42, 12.88, 6.44, and 3.22 ms. The reference AGFA 5°, 95 % backazimuth limit remains approximately 2.992 ms because the arrival-time directional estimator is not frequency indexed, whereas the independent-error monochromatic $C_B \geq 0.90$ limits are approximately 51.66, 10.33, 5.17, and 2.58 ms.

https://doi.org/10.5194/egusphere-2026-5154
Preprint. Discussion started: 2 November 2026
© Author(s) 2026. CC BY 4.0 License.

These values can be displayed on a common temporal axis, but they are not estimates of a common timing-error random variable. The spectral-phase criterion acts on single-path residual timing, the polarisation criterion on E-channel timing relative to synchronised N/Z, the backazimuth criterion on independent station timing errors projected through array geometry, and the beam criterion on pairwise inter-station phase coherence. Differential-delay admissibility introduces another pairwise timing variable whose dependence on covariance is shown separately in Fig. 3. The numerical ordering of the task-specific limits therefore changes with frequency, geometry, topology, and selected performance criterion rather than converging towards a unique timing-accuracy threshold.

Taken together, the results establish three principal properties of timing admissibility across the investigated benchmarks. First, admissibility is observable dependent: spectral phase, differential delay, three-component polarisation, array backazimuth, and coherent beamforming respond to different timing-error variables and therefore impose different conditional bounds. Second, marginal timing variance alone is insufficient to characterise multichannel or multistation performance because common-mode and differential components propagate differently into relative observables. Third, receiver geometry, wavefield properties, frequency content, and processing choices can shift admissible timing scales even when nominal timing-error magnitude and performance criterion are otherwise held fixed. The numerical experiments therefore identify task- and topology-specific admissible regions rather than a universal timing requirement.

6 Discussion

The results demonstrate that timing admissibility is not an intrinsic scalar property of a seismic station or network, but a conditional property of the complete measurement operator. The same nominal timing-error scale produces markedly different consequences when propagated into spectral phase, differential delay, three-component polarisation, array backazimuth, or coherent beam formation. This distinction is not merely quantitative. The relevant timing variable itself changes among tasks: a single-path residual timing error controls spectral phase, pairwise differential timing controls differential delay, intercomponent relative timing controls polarisation, independent or structured interstation timing errors perturb slowness estimation, and pairwise differential timing controls coherent beam retention. A timing specification expressed only as a station-wise standard deviation therefore suppresses information that is essential for predicting measurement performance.

Operational seismic networks may characterise timing quality through synchronisation metrics or nominal design targets. The Global Seismographic Network (GSN), for example, was designed with a goal of reported timing better than 10 ms, and an extensive assessment of collocated GSN sensors found mean timing differences below approximately 10 ms when clock quality was not compromised (Ringler et al., 2021). Historical and network-wide analyses nevertheless show that timing failures can span from tens of milliseconds to seconds and may remain incompletely represented by quality metadata (Agnew, 2020; Yang et al., 2022; see also Yang et al., 2024). The present results do not imply that such network specifications are inappropriate. Rather, they show why a nominal value such as 10 ms cannot, by itself, establish suitability for every downstream observable. In the benchmarks considered here, a 10 ms uncertainty is weakly consequential for some low-frequency or large-aperture measurements but exceeds the adopted admissibility criterion for several high-frequency phase, polarisation, compact-array, and coherence measurements.

The distinction between absolute and differential timing is particularly important. A constant timing displacement, or one that is effectively common over the relevant measurement interval, can be severe in absolute time while remaining invisible to observables constructed from simultaneous interstation differences. Conversely, relatively small differential timing errors can strongly affect phase-sensitive measurements even when the absolute clocks remain close to a reference standard. This invariance does not extend automatically to a common timing process that evolves appreciably over the temporal separation entering the observable. The distinction is consistent with approaches that infer station timing errors from interstation correlations: pairwise observations constrain relative clock differences, whereas recovery of absolute network time requires an external or otherwise trusted reference (Sens-Schönfelder, 2008). Subsequent studies have demonstrated the practical recovery of clock drift and timing offsets from ambient-noise correlations in both terrestrial and ocean-bottom deployments (Hable et al., 2018; Weemstra et al., 2021). The covariance experiments in Fig. 6 extend this distinction from correction to admissibility: even at identical marginal σ_t, the expected measurement degradation depends directly on how timing errors are shared among stations.

https://doi.org/10.5194/egusphere-2026-5154
Preprint. Discussion started: 2 November 2026
© Author(s) 2026. CC BY 4.0 License.

This point also connects seismological timing requirements to frequency metrology. Allan variance and related stability measures provide a rigorous description of oscillator fluctuations as a function of averaging time and noise process (Allan, 1966; Barnes et al., 1971). Such metrics characterise the clock or oscillator itself, but they do not specify the impact of that instability on a particular seismic estimator. The framework developed here occupies the subsequent stage of that chain: a timing-error process, whether represented deterministically, statistically, or through a covariance model, is propagated into a task-specific observable and evaluated against an explicit performance criterion. In this sense, oscillator stability and seismic admissibility are complementary rather than interchangeable concepts. A future operational implementation could combine measured Allan-deviation behaviour with an explicit stochastic clock model and assumptions about common versus differential timing structure to construct measurement-window-dependent timing covariance models, which could then be propagated through the task-specific operators considered here.

The polarisation results emphasise an additional distinction between station timing and intercomponent timing. Conventional station clock quality primarily describes the temporal reference shared by a data logger, whereas polarisation depends on relative phase among orthogonal components. Component-dependent effective delays may therefore arise from mechanisms other than failure of the master clock, including imperfectly known response phase or erroneous response correction, which can generate frequency-dependent apparent timing errors (Weemstra et al., 2021). Accordingly, the E-only perturbations used in Figs. 4 and 7 should be interpreted as controlled effective intercomponent timing residuals, not exclusively as literal independent clock errors between components. The principal result is that the polarisation operator is sensitive to such residuals; the experiment does not diagnose their instrumental origin.

The large contrast between the timing tolerances of the 10 km synthetic arrays and the compact AGFA geometry further demonstrates why aperture cannot be omitted from timing specifications. Arrival-time perturbations map into slowness error through the spatial design matrix, so the same absolute timing perturbation represents a much larger fraction of the propagation delay across a compact array than across a large-aperture array. The dependence on backazimuth within the fixed AGFA geometry additionally shows that aperture expressed by a single scalar radius is insufficient: orientation and conditioning of the receiver distribution relative to the incoming slowness vector also matter. This behaviour is consistent with the established geometric basis of seismic-array resolution and slowness estimation (Rost and Thomas, 2002), but the present analysis makes its timing consequence explicit by expressing the result directly as an admissible timing scale. The values derived for the synthetic and AGFA configurations should therefore not be interpreted as competing estimates of a general array requirement; they quantify different geometrical measurement operators.

The RJOB experiment provides a complementary test of the analytical and idealised polarisation calculations. Its significance is not that one waveform establishes an empirical timing requirement for earthquake polarisation analysis. Rather, it shows that controlled intercomponent timing perturbations remain observable when the ideal monochromatic wavefield is replaced by a real, spectrally structured three-component recording. The strong band dependence and the sensitivity of exact angular errors to window and taper selection also illustrate why waveform-dependent estimators cannot generally be assigned a timing threshold solely from nominal centre frequency. At the same time, the processing ensemble shows that the qualitative conclusion survives reasonable perturbations of the analysis window: timing response remains task and band dependent even when all other aspects of the recorded waveform are held fixed. Because the RJOB responses were not corrected for instrument response and only one observational segment was used, these results are appropriately interpreted as a reproducibility benchmark rather than as population-level evidence.

The comparison among the four task-specific criteria in Fig. 8 is therefore most informative when viewed as a topology comparison rather than as a ranking of applications. The spectral-phase criterion acts on a single residual delay; polarisation acts on one component relative to the others; backazimuth acts on a vector of station timing errors projected through array geometry; and beam coherence depends on pairwise timing differences. Their numerical thresholds cannot be collapsed into a single ordering without first defining how the underlying timing-error variables are related. This is also why the perfectly common-mode case can be fully admissible for relative beam coherence while remaining potentially unacceptable for tasks requiring absolute timing. The differential-delay benchmark in Fig. 3 provides a fifth example of the same principle: its native error variable is a pairwise timing difference whose admissibility depends explicitly on timing covariance. A universal “minimum timing accuracy” would therefore conflate distinct error spaces.

An operational implication is that seismic timing quality could be reported more usefully as a hierarchy of descriptors rather than through a single scalar flag. Existing quality-control systems already provide valuable

https://doi.org/10.5194/egusphere-2026-5154
Preprint. Discussion started: 2 November 2026
© Author(s) 2026. CC BY 4.0 License.

information on synchronisation status and timing quality, and network-wide evaluations demonstrate the importance of such metadata (Ringler et al., 2021; Yang et al., 2022). The present results suggest that, where technically feasible, this information could be supplemented by estimates of residual timing variance, evidence for common-mode versus differential structure, relevant correlation times or spatial correlation scales, and the frequency range over which the estimate applies. This proposal should be regarded as an instrumentation and metadata implication of the framework rather than as a validated operational standard. Its practical value would need to be assessed against the telemetry, calibration, and quality-control capabilities of specific network architectures.

The same distinction is relevant to autonomous and ocean-bottom deployments, where clock behaviour can evolve substantially between external synchronisations. Ambient-noise methods have demonstrated that clock errors and clock drift can be reconstructed from seismic data themselves (Sens-Schönfelder, 2008; Hable et al., 2018; Weemstra et al., 2021). Recent OBS studies further show that timing behaviour can remain challenging over large apertures and long deployments (Cabieces et al., 2024), while explicitly nonlinear clock evolution can make a simple endpoint-based linear drift correction inadequate for some instruments (Schmidt-Aursch et al., 2026). The framework developed here addresses a different but complementary question: once residual timing uncertainty remains after synchronisation or correction, how large can that uncertainty be before a specified seismic measurement becomes inadmissible? Clock-correction methods and task-dependent admissibility analysis can therefore be treated as consecutive stages of the same quality-control chain.

Several limitations delimit the interpretation of the numerical thresholds. The stochastic benchmarks assume zero-mean Gaussian residual timing errors except where deterministic offsets or gradients are imposed. Real clock behaviour can include drift, jumps, missing samples, nonlinear thermal effects, ageing, and temporally correlated processes; such behaviour has been documented in both land and ocean-bottom seismic deployments (Hable et al., 2018; Yang et al., 2022; Cabieces et al., 2024; Schmidt-Aursch et al., 2026). Gaussian covariance propagation should therefore be understood as a controlled local model of residual timing uncertainty rather than as a complete stochastic model of clock failure. Heavy-tailed, discontinuous, or strongly non-stationary timing processes would require their own propagation laws and could yield substantially different exceedance probabilities.

A second limitation is that the benchmarks intentionally isolate timing from several interacting sources of seismic measurement error. Phase picking and association are treated as correct; propagation velocity and slowness models are fixed; sensor orientation, response uncertainty, additive noise, waveform distortion, site response, and source complexity are not jointly marginalised. In operational data, these terms can be correlated with timing or can produce signatures that partially resemble timing perturbations. In particular, frequency-dependent response-phase errors can appear as effective delays over restricted bands, whereas propagation-model errors can bias relative arrival times in arrays. The present framework therefore establishes conditional timing sensitivity, not a complete error budget. Extension to joint covariance or hierarchical uncertainty models would be required before assigning timing a unique fraction of the uncertainty observed in field measurements.

A third limitation concerns the scope of the observational and geometrical benchmarks. The RJOB test uses one public three-component waveform, and the AGFA analysis uses one compact five-station geometry. These choices provide transparent and reproducible stress tests but do not sample the diversity of source mechanisms, incidence angles, noise environments, array apertures, station counts, or network geometries encountered in operational seismology. The sensitivity experiments partly address this limitation, but broader validation should include multiple event classes, regional and teleseismic wavefields, permanent and temporary arrays, and timing-error distributions estimated directly from network quality-control records. Such an extension would allow the framework to move from controlled admissibility maps towards empirical task-specific timing-risk distributions.

Despite these limitations, the central inference is robust across the analytical, synthetic, and observational components of the study: timing quality becomes physically meaningful only after the relevant error topology and measurement operator have been specified. Single-path residual timing, pairwise differential timing, intercomponent skew, independent station error, spatially correlated timing error, and common-mode error are not interchangeable descriptions of a timing problem. Likewise, spectral phase, differential delay, polarisation, backazimuth, and beam coherence do not impose interchangeable timing requirements. The practical consequence is that synchronisation performance should be evaluated forward from the timing process to the intended seismic observable, rather than backward from a single generic millisecond specification.

https://doi.org/10.5194/egusphere-2026-5154
Preprint. Discussion started: 2 November 2026
© Author(s) 2026. CC BY 4.0 License.

7 Conclusions

This study has formulated timing quality in digital seismology as a task-dependent measurement-admissibility problem rather than as a universal property of clock performance. The framework separates the temporal evolution of timing error from its spatial or channel topology and covariance, and propagates these quantities through the measurement operator associated with the seismic observable of interest. This distinction is essential because timing perturbations having the same nominal amplitude can produce fundamentally different consequences depending on whether they act as single-path residual delays, pairwise differential errors, intercomponent skew, independent station errors, spatially structured timing fields, or common-mode perturbations.

The analytical and controlled numerical results show that spectral phase, differential delay, three-component polarisation, array slowness and backazimuth, and coherent beamforming define different conditional timing-admissibility bounds. Single-path phase sensitivity scales directly with frequency, whereas differential-delay admissibility depends additionally on covariance between timing states. Polarisation is governed by relative intercomponent timing and can exhibit nonlinear and non-monotonic responses to timing skew. In arrays, an array-common timing offset can be absorbed by the fitted intercept, while a spatially linear timing gradient is exactly confounded with a slowness perturbation under the adopted plane-wave model. In the timing-only formulation, beam coherence is controlled by pairwise timing differences and therefore remains unaffected by perfectly common-mode timing uncertainty, even when absolute timing is poor.

The controlled synthetic, observational, and public-array benchmarks further show that admissible timing scales depend on receiver geometry, wavefield properties, frequency content, processing choices, and the probability or performance criterion adopted for the measurement. The RJOB waveform experiment demonstrates that intercomponent timing sensitivity persists in a spectrally structured observational record, while the synthetic-array and compact AGFA benchmarks together demonstrate the dependence of array-direction admissibility on receiver geometry and incident slowness. These experiments are intended as reproducible forward-propagation benchmarks rather than empirical estimates of the timing performance of operational seismic networks.

The principal implication is that a single millisecond specification cannot, in general, establish whether a seismic recording system is adequate for every downstream measurement. Timing specifications and quality-control metadata are most informative when interpreted together with the relevant error topology, covariance structure, frequency range, and measurement task. Clock stability metrics, synchronisation diagnostics, and timing-correction procedures therefore provide necessary inputs to seismic data-quality assessment, but their scientific significance emerges only after the residual timing uncertainty is propagated into the intended observable.

The framework developed here provides a basis for that forward evaluation. Its present implementation deliberately isolates timing from several other sources of measurement uncertainty and uses controlled Gaussian residual models for most stochastic benchmarks. Future extensions should incorporate empirically estimated clock-noise processes, non-Gaussian and non-stationary timing errors, joint timing–response–orientation–propagation uncertainty, and broader observational and network geometries. Within these limitations, the central result is robust: timing admissibility is conditional on both the structure of the timing error and the seismic task through which that error is observed, and should therefore be evaluated through the complete measurement operator rather than through a universal clock-accuracy threshold.

Appendix A: Timing-to-slowness propagation for a planar array

For completeness, the timing-to-slowness mapping used in Sect. 3 is derived here from the weighted least-squares plane-wave model. Consider M stations with horizontal coordinates collected in the matrix $\mathbf{G} \in \mathbb{R}^{M\times 2}$, and let $\mathbf{1}$ denote the M-component vector of ones. The observed arrival-time vector is represented by the augmented linear model

$$\mathbf{t} = \mathbf{A}\boldsymbol{\theta} + \boldsymbol{\delta t}, \qquad \mathbf{A} = [\mathbf{1} \quad \boldsymbol{G}], \qquad \boldsymbol{\theta} = \begin{bmatrix} t_0 \\ \mathbf{p} \end{bmatrix}, \tag{A1}$$

where t_0 is the fitted intercept, $\mathbf{p} = (p_E, p_N)^{\mathrm{T}}$ is the horizontal slowness vector, and $\boldsymbol{\delta t}$ contains the station timing perturbations. Let W be a symmetric positive-definite matrix of deterministic fitting weights. Provided that A has full column rank, the weighted least-squares estimator gives

https://doi.org/10.5194/egusphere-2026-5154
Preprint. Discussion started: 2 November 2026
© Author(s) 2026. CC BY 4.0 License.

$$\widehat{\boldsymbol{\theta}} - \boldsymbol{\theta} = \left(\mathbf{A}^{\mathrm{T}}\mathbf{W}\mathbf{A}\right)^{-1}\mathbf{A}^{\mathrm{T}}\mathbf{W}\boldsymbol{\delta t}. \qquad \text{(A2)}$$

Thus, timing error enters the estimated intercept and horizontal slowness through a linear projection determined by the receiver geometry and the adopted weighting.

The intercept can be separated explicitly from the slowness terms by centring the receiver coordinates with respect to the weights. Define the weighted coordinate centroid and centred geometry matrix as

$$\bar{\mathbf{r}}_W^{\mathrm{T}} = \frac{\mathbf{1}^{\mathrm{T}}\mathbf{W}\mathbf{G}}{\mathbf{1}^{\mathrm{T}}\mathbf{W}\mathbf{1}}, \quad \mathbf{G}_c = \mathbf{G} - \mathbf{1}\,\bar{\mathbf{r}}_W^{\mathrm{T}}, \quad \mathbf{1}^{\mathrm{T}}\mathbf{W}\mathbf{G}_c = \mathbf{0}^{\mathrm{T}}. \qquad \text{(A3)}$$

With this centring, the intercept and slowness blocks of the weighted normal matrix are orthogonal. The slowness perturbation obtained from Eq. (A2) therefore reduces to

$$\Delta\mathbf{p} = \mathbf{H}\boldsymbol{\delta t}, \quad \mathbf{H} = \left(\mathbf{G}_c^{\mathrm{T}}\mathbf{W}\mathbf{G}_c\right)^{-1}\mathbf{G}_c^{\mathrm{T}}\mathbf{W}. \qquad \text{(A4)}$$

Equation (A4) is the timing-to-slowness operator used in Eq. (35) of the main text. When the receiver coordinates have already been centred with respect to the adopted weights, $\mathbf{G}_c = \mathbf{G}$, giving directly the form used there. Because $\mathbf{G}_c^{\mathrm{T}}\mathbf{W}\mathbf{1} = \mathbf{0}$, Eq. (A4) also gives $\mathbf{H}\mathbf{1} = \mathbf{0}$. An array-common constant timing displacement is therefore absorbed by the fitted intercept and produces no slowness bias.

The complementary case is a timing perturbation containing a spatially linear component across the array. In centred coordinates, let

$$\boldsymbol{\delta t} = b\,\mathbf{1} + \mathbf{G}_c\mathbf{g}, \qquad \text{(A5)}$$

where b is an array-common timing offset and $\mathbf{g} = (g_E, g_N)^{\mathrm{T}}$ is a horizontal timing gradient with units of time per unit distance. Substitution of Eq. (A5) into Eq. (A4) gives

$$\Delta\mathbf{p} = \mathbf{H}(b\,\mathbf{1} + \mathbf{G}_c\mathbf{g}) = \mathbf{g}, \qquad \text{(A6)}$$

provided that $\mathbf{G}_c$ has rank two. A spatially linear timing gradient is therefore exactly degenerate with an equal horizontal slowness perturbation under the adopted planar plane-wave model. This result is independent of array shape for any full-rank geometry when the gradient component of the imposed timing field lies exactly in the column space of $\mathbf{G}_c$; the constant component is absorbed by the fitted intercept. Receiver geometry becomes relevant for timing components that do not satisfy this exact deterministic relation and for stochastic timing uncertainty.

For a zero-mean timing-error vector with covariance $\boldsymbol{\Sigma}_t$, Eq. (A4) gives the general propagation relation

$$\boldsymbol{\Sigma}_p = \mathbf{H}\boldsymbol{\Sigma}_t\mathbf{H}^{\mathrm{T}},$$

as stated in Eq. (38) of the main text. In the particular case of independent station timing errors with common variance σ_t^2, the covariance becomes

$$\begin{aligned} \boldsymbol{\Sigma}_p &= \sigma_t^2\mathbf{H}\mathbf{H}^{\mathrm{T}} \\ &= \sigma_t^2\left(\mathbf{G}_c^{\mathrm{T}}\mathbf{W}\mathbf{G}_c\right)^{-1}\mathbf{G}_c^{\mathrm{T}}\mathbf{W}\mathbf{W}^{\mathrm{T}}\mathbf{G}_c\left(\mathbf{G}_c^{\mathrm{T}}\mathbf{W}\mathbf{G}_c\right)^{-1}, \qquad \text{(A7)} \\ \mathbf{W} \propto \mathbf{I} \implies \boldsymbol{\Sigma}_p &= \sigma_t^2\left(\mathbf{G}_c^{\mathrm{T}}\mathbf{G}_c\right)^{-1}. \end{aligned}$$

The equal-weight result makes the role of receiver geometry explicit. Larger spatial leverage reduces the overall propagation of independent station timing variance into slowness uncertainty, whereas directional conditioning controls its anisotropy and the amplification along weakly resolved slowness directions.

Appendix B: Gaussian timing covariance and expected beam coherence

https://doi.org/10.5194/egusphere-2026-5154
Preprint. Discussion started: 2 November 2026
© Author(s) 2026. CC BY 4.0 License.

The beam-coherence expressions used in Sect. 3 are derived here for a correctly steered narrow-band plane wave affected only by residual station timing errors. After removal of the nominal geometric phase delays and normalisation to unit station amplitude, the residual complex beam at frequency f is

$$B(f) = \frac{1}{M}\sum_{i=1}^{M} \exp(-\mathrm{i}\, 2\pi f\, \delta t_i)\,, \qquad \text{(B1)}$$

where δt_i is the residual timing error at station i. This timing-only representation isolates the loss of coherent summation caused by differential phase perturbations and excludes amplitude errors, sensor-response mismatch, propagation-model error, and additive noise.
The corresponding normalised beam power is

$$|B(f)|^2 = \frac{1}{M^2}\sum_{i=1}^{M}\sum_{j=1}^{M} \exp\left[-\mathrm{i}\, 2\pi f\left(\delta t_i - \delta t_j\right)\right]. \qquad \text{(B2)}$$

The diagonal terms $i = j$ are identically equal to unity. The off-diagonal terms depend only on pairwise differential timing and therefore contain no contribution from an exactly common timing displacement.
Let the timing-error vector $\boldsymbol{\delta t} = (\delta, t_1, \ldots \delta t_M)^{\mathrm{T}}$ be zero-mean multivariate Gaussian with covariance matrix $\boldsymbol{\Sigma}_t$. For each station pair,

$$\begin{aligned} \mathrm{Var}\left(\delta t_i - \delta t_j\right) &= \Sigma_{t,ii} + \Sigma_{t,jj} - 2\Sigma_{t,ij}, \\ \mathbb{E}\left\{\exp\left[-\mathrm{i}\, 2\pi f\left(\delta t_i - \delta t_j\right)\right]\right\} &= \exp\left[-2\pi^2 f^2\left(\Sigma_{t,ii} + \Sigma_{t,jj} - 2\Sigma_{t,ij}\right)\right]. \end{aligned} \qquad \text{(B3)}$$

The second relation follows directly from the characteristic function of a zero-mean Gaussian variable. It shows explicitly that coherence loss is governed by the variance of pairwise timing differences rather than by marginal station timing variance alone.
Averaging Eq. (B3) over all ordered off-diagonal station pairs defines the expected pairwise coherence-retention factor,

$$C_B(f) = \frac{1}{M(M-1)}\sum_{i\neq j} \exp\left[-2\pi^2 f^2\left(\Sigma_{t,ii} + \Sigma_{t,jj} - 2\Sigma_{t,ij}\right)\right]. \qquad \text{(B4)}$$

This is Eq. (39) of the main text. The quantity C_B is a timing-induced pairwise phase-coherence retention factor, not a conventional magnitude-squared spectral-coherence estimator.
Substitution of Eq. (B4) into Eq. (B2) gives

$$\mathbb{E}[|\, B(f)\,|^2] = \frac{1}{M} + \left(1 - \frac{1}{M}\right) C_B(f), \qquad \text{(B5)}$$

which recovers Eq. (40) of the main text. The first term is contributed by the M self-pairs, whereas the second contains the $M(M-1)$ cross-station pairs. Accordingly, C_B isolates the relative phase coherence of distinct stations, while $\mathbb{E}[|\, B\,|^2]$ retains the finite-M self-power term.
For the equicorrelated covariance model, $\boldsymbol{\Sigma}_t = \sigma_t^2[(1-\rho)\mathbf{I} + \rho\, \mathbf{1}\mathbf{1}^{\mathrm{T}}]$, positive semidefiniteness for M stations requires $-1/(M-1) \le \rho \le 1$. The controlled benchmarks in Fig. 6 use the non-negative part of this range. All off-diagonal timing differences then have variance $2\sigma_t^2(1-\rho)$, and Eqs. (B4)–(B5) reduce to

$$\begin{aligned} C_B(f) &= \exp[-4\pi^2 f^2 \sigma_t^2 (1-\rho)]\,, \\ \mathbb{E}[|\, B(f)\,|^2] &= \frac{1}{M} + \left(1 - \frac{1}{M}\right)\exp[-4\pi^2 f^2 \sigma_t^2 (1-\rho)]\,, \\ \rho = 0 &\Rightarrow C_B(f) = \exp(-4\pi^2 f^2 \sigma_t^2)\,, \\ \rho = 1 &\Rightarrow C_B(f) = 1,\ \mathbb{E}[|\, B(f)\,|^2] = 1. \end{aligned} \qquad \text{(B6)}$$

https://doi.org/10.5194/egusphere-2026-5154
Preprint. Discussion started: 2 November 2026
© Author(s) 2026. CC BY 4.0 License.

Thus, independent timing errors produce coherence loss that increases with both frequency and marginal timing variance, whereas positive common structure reduces pairwise differential variance and therefore preserves a larger fraction of the inter-station coherence. Within the admissible range of the equicorrelated model, negative correlation has the opposite effect: it increases pairwise differential variance and therefore produces stronger coherence loss than the independent case at fixed marginal σ_t. In the limiting perfectly common-mode case, all stations acquire the same residual phase and the timing-only beam retains unit relative coherence and unit normalised power. This does not imply correct absolute timing: the entire array may remain displaced from the reference time while relative beam coherence is unaffected.

The same general relation applies to non-equicorrelated covariance structures, including the spatial exponential model used in Fig. 6. In that case, each station pair contributes according to its own differential timing variance through Eq. (B4), so receiver geometry enters the expected coherence through the distribution of inter-station separations and the corresponding covariance values. Arrays with identical station-wise marginal variance and comparable overall aperture can therefore retain different coherence when their timing errors are spatially correlated.

The broadband independent-error expression used in Fig. 8d follows directly by evaluating the independent special case of Eq. (B6) at the discrete spectral frequencies and averaging the resulting $C_B(f_k)$ values with the normalised empirical spectral weights defined in Eqs. (45)–(46). The broadband calculation therefore changes the spectral aggregation but not the underlying dependence of coherence on pairwise differential timing variance.

Code and data availability

All numerical experiments, analytical benchmarks, figure-generation workflows, and derived numerical outputs used in this study were implemented in Python. The complete reproducibility package, including the scripts required to reproduce the analytical and synthetic calculations, the numerical data underlying the figures, and the associated configuration information, will be archived in a FAIR-aligned public repository after acceptation. The corresponding persistent identifier will be inserted here and cited in the reference list once the archive has been finalised.

The observational three-component waveform used for the controlled RJOB perturbation benchmark is publicly distributed with the ObsPy example data and is documented in the ObsPy picker tutorial. The record comprises the north, east, and vertical components used in Sect. 4 and Fig. 7; the reference P- and S-arrival markers employed in the processing benchmark are those returned by the documented ObsPy autoregressive-picker example. ObsPy itself is described by Beyreuther et al. (2010), Megies et al. (2011), and Krischer et al. (2015).

The compact five-station geometry used in the AGFA benchmark of Fig. 8 is derived from the public ObsPy FK-analysis example, which uses data from the demolition of the AGFA skyscraper in Munich and explicitly provides the five receiver coordinates used by the example array. Only the public receiver geometry is used here; the wavefield, timing gradient, and stochastic timing perturbations analysed in this study are controlled synthetic constructions defined in Sect. 4.

No proprietary seismic data, restricted-access network products, or confidential calibration information are required to reproduce the results. The remaining synthetic receiver geometries, timing-error realisations, covariance models, spectral weights derived for the controlled benchmarks, and all quantities plotted in Figs. 1–8 are either generated deterministically by the archived scripts or supplied as machine-readable files in the reproducibility package.

Supplement link

The supplement related to this article is available online at: [link to be inserted by Copernicus].

Author contribution

The author was solely responsible for the conceptualization, methodology, software development, validation, formal analysis, investigation, data curation, visualization, and interpretation of the study, as well as for writing the original draft and reviewing and editing the manuscript.

https://doi.org/10.5194/egusphere-2026-5154
Preprint. Discussion started: 2 November 2026
© Author(s) 2026. CC BY 4.0 License.

Competing interests
The author declares that there is no conflict of interest.

Acknowledgements
The author acknowledges the developers and maintainers of ObsPy for providing the open-source software, example waveform data, and public array information used in the reproducibility benchmarks presented in this study.

Financial support
This research received no specific grant from any funding agency in the public, commercial, or not-for-profit sectors.

References
Agnew, D. C.: Time marks and clock corrections: A century of seismological timekeeping, Seismol. Res. Lett., 91, 1417–1429, https://doi.org/10.1785/0220190284, 2020.

Allan, D. W.: Statistics of atomic frequency standards, Proc. IEEE, 54, 221–230, https://doi.org/10.1109/PROC.1966.4634, 1966.

Barnes, J. A., Chi, A. R., Cutler, L. S., Healey, D. J., Leeson, D. B., McGunigal, T. E., Mullen Jr., J. A., Smith, W. L., Sydnor, R. L., Vessot, R. F. C., and Winkler, G. M. R.: Characterisation of frequency stability, IEEE Trans. Instrum. Meas., IM-20, 105–120, https://doi.org/10.1109/TIM.1971.5570702, 1971.

Beyreuther, M., Barsch, R., Krischer, L., Megies, T., Behr, Y., and Wassermann, J.: ObsPy: A Python toolbox for seismology, Seismol. Res. Lett., 81, 530–533, https://doi.org/10.1785/gssrl.81.3.530, 2010.

Cabieces, R., Harris, K., Ferreira, A. M. G., Tsekhmistrenko, M., Hicks, S. P., Krüger, F., Geissler, W. H., Hannemann, K., and Schmidt-Aursch, M. C.: Clock drift corrections for large aperture ocean bottom seismometer arrays: Application to the UPFLOW array in the mid-Atlantic Ocean, Geophys. J. Int., 239, 1709–1728, https://doi.org/10.1093/gji/ggae354, 2024.

Capon, J.: High-resolution frequency-wavenumber spectrum analysis, Proc. IEEE, 57, 1408–1418, https://doi.org/10.1109/PROC.1969.7278, 1969.

D'Alessandro, A.: Causal and uncertainty-aware digital-twin framework for ultra–low-noise geoscientific inertial sensors, Geosci. Instrum. Method. Data Syst., 15, 195–211, https://doi.org/10.5194/gi-15-195-2026, 2026a.

D'Alessandro, A.: Causal and uncertainty-aware instrument correction in broad-band seismology: Minimum-phase inversion, discretization effects and self-noise performance bounds, Geophys. J. Int., 246, ggag265, https://doi.org/10.1093/gji/ggag265, 2026b.

Gibbons, S. J.: On the identification and documentation of timing errors: An example at the KBS station, Spitsbergen, Seismol. Res. Lett., 77, 559–571, https://doi.org/10.1785/gssrl.77.5.559, 2006.

Gouédard, P., Seher, T., McGuire, J. J., Collins, J. A., and van der Hilst, R. D.: Correction of ocean-bottom seismometer instrumental clock errors using ambient seismic noise, Bull. Seismol. Soc. Am., 104, 1276–1288, https://doi.org/10.1785/0120130157, 2014.

https://doi.org/10.5194/egusphere-2026-5154
Preprint. Discussion started: 2 November 2026
© Author(s) 2026. CC BY 4.0 License.

Hable, S., Sigloch, K., Barruol, G., Stähler, S. C., and Hadziioannou, C.: Clock errors in land and ocean bottom seismograms: High-accuracy estimates from multiple-component noise cross-correlations, Geophys. J. Int., 214, 2014–2034, https://doi.org/10.1093/gji/ggy236, 2018.

Hannemann, K., Krüger, F., and Dahm, T.: Measuring of clock drift rates and static time offsets of ocean bottom stations by means of ambient noise, Geophys. J. Int., 196, 1034–1042, https://doi.org/10.1093/gji/ggt434, 2014.

Hirose, T. and Ueda, H.: Continuous monitoring of instrumental clock errors at 50 volcanoes in Japan based on seismic interferometry, Earth Planets Space, 75, 50, https://doi.org/10.1186/s40623-023-01798-4, 2023.

Joint Committee for Guides in Metrology (JCGM): Evaluation of measurement data – Guide to the expression of uncertainty in measurement, JCGM 100:2008(E), https://doi.org/10.59161/JCGM100-2008E, 2008a.

Joint Committee for Guides in Metrology (JCGM): Evaluation of measurement data – Supplement 1 to the "Guide to the expression of uncertainty in measurement" – Propagation of distributions using a Monte Carlo method, JCGM 101:2008, https://doi.org/10.59161/JCGM101-2008, 2008b.

Joint Committee for Guides in Metrology (JCGM): International Vocabulary of Metrology – Basic and general concepts and associated terms (VIM), 3rd edn., JCGM 200:2012, https://doi.org/10.59161/JCGM200-2012, 2012.

Joint Committee for Guides in Metrology (JCGM): Guide to the expression of uncertainty in measurement – Part 6: Developing and using measurement models, JCGM GUM-6:2020, https://doi.org/10.59161/JCGMGUM-6-2020, 2020.

Jurkevics, A.: Polarisation analysis of three-component array data, Bull. Seismol. Soc. Am., 78, 1725–1743, https://doi.org/10.1785/BSSA0780051725, 1988.

Krischer, L., Megies, T., Barsch, R., Beyreuther, M., Lecocq, T., Caudron, C., and Wassermann, J.: ObsPy: A bridge for seismology into the scientific Python ecosystem, Comput. Sci. Discov., 8, 014003, https://doi.org/10.1088/1749-4699/8/1/014003, 2015.

Lecointre, A., Roux, P., Bouttier, P.-A., Picard, C., and Louvet, V.: A graph approach for fast dense array inter-station phase delay interpretation, Geophys. J. Int., 235, 1260–1273, https://doi.org/10.1093/gji/ggad301, 2023.

Maranò, S. and Fäh, D.: Processing of translational and rotational motions of surface waves: Performance analysis and applications to single sensor and to array measurements, Geophys. J. Int., 196, 317–339, https://doi.org/10.1093/gji/ggt187, 2014.

Megies, T., Beyreuther, M., Barsch, R., Krischer, L., and Wassermann, J.: ObsPy – What can it do for data centers and observatories?, Ann. Geophys., 54, 47–58, https://doi.org/10.4401/ag-4838, 2011.

Riley, W. J.: Handbook of frequency stability analysis, NIST Special Publication 1065, National Institute of Standards and Technology, https://doi.org/10.6028/NIST.SP.1065, 2008.

Ringler, A. T., Anthony, R. E., Wilson, D. C., Auerbach, D., Bargabus, S., Davis, P. W., Gunnels, M., Hafner, K., Holland, J., Kearns, A., and Klimczak, E.: A review of timing accuracy across the Global Seismographic Network, Seismol. Res. Lett., 92, 2270–2281, https://doi.org/10.1785/0220200394, 2021.

Ringler, A. T., Anthony, R. E., Aster, R. C., Ammon, C. J., Arrowsmith, S., Benz, H. M., Ebeling, C., Frassetto, A., Kim, W. Y., Koelemeijer, P., Lau, H. C. P., Lekic, V., Montagner, J. P., Richards, P. G., Schaff, D. P., Vallee, M., and Yeck, W. L.: Achievements and prospects of global broadband seismographic networks after 30 years

© Author(s) 2026. CC BY 4.0 License.

of continuous geophysical observations, Rev. Geophys., 60, e2021RG000749, https://doi.org/10.1029/2021RG000749, 2022.

Ringler, A. T., Anthony, R. E., Bastien, P., Pascale, A., and Merchant, B. J.: Introduction to the digitization of seismic data: A user's guide, Seismol. Res. Lett., 94, 2060–2074, https://doi.org/10.1785/0220220158, 2023.

Röhm, A. H. E., Bijwaard, H., Spakman, W., and Trampert, J.: Effects of arrival time errors on traveltime tomography, Geophys. J. Int., 142, 270–276, https://doi.org/10.1046/j.1365-246X.2000.00145.x, 2000.

Rost, S. and Thomas, C.: Array seismology: Methods and applications, Rev. Geophys., 40, 1008, https://doi.org/10.1029/2000RG000100, 2002.

Schmidt-Aursch, M. C., Almendros, J., Geissler, W. H., Heit, B., and Yuan, X.: Correction of nonlinear clock drift: The BRAVOSEIS Ocean-Bottom Seismometer Network in the Bransfield Strait, Antarctica, Geophys. J. Int., 245, ggag064, https://doi.org/10.1093/gji/ggag064, 2026.

Sens-Schönfelder, C.: Synchronizing seismic networks with ambient noise, Geophys. J. Int., 174, 966–970, https://doi.org/10.1111/j.1365-246X.2008.03842.x, 2008.

Song, J., Zhu, G., Li, Q., and Zhang, Y.: A wavefield-domain method for refining residual timing errors in passive-source seismic exploration, Sensors, 26, 3567, https://doi.org/10.3390/s26113567, 2026.

Stehly, L., Campillo, M., and Shapiro, N. M.: Traveltime measurements from noise correlation: Stability and detection of instrumental time-shifts, Geophys. J. Int., 171, 223–230, https://doi.org/10.1111/j.1365-246X.2007.03492.x, 2007.

Syracuse, E. M., Phillips, W. S., Maceira, M., and Begnaud, M. L.: Identifying and correcting timing errors at seismic stations in and around Iran, Seismol. Res. Lett., 88, 1472–1479, https://doi.org/10.1785/0220170113, 2017.

Tian, J., Lin, J., Zhang, F., Xu, M., Zhang, Y., Guo, L., and Zeng, X.: Time correction of ocean-bottom seismometers using improved ambient noise cross correlation of multicomponents and dual-frequency bands, Seismol. Res. Lett., 92, 2004–2014, https://doi.org/10.1785/0220200358, 2021.

Vidale, J. E.: Complex polarisation analysis of particle motion, Bull. Seismol. Soc. Am., 76, 1393–1405, https://doi.org/10.1785/BSSA0760051393, 1986.

Wassermann, J., Lehndorfer, S., Igel, H., and Schreiber, U.: Performance test of a commercial rotational motions sensor, Bull. Seismol. Soc. Am., 99, 1449–1456, https://doi.org/10.1785/0120080157, 2009.

Weemstra, C., de Laat, J. I., Verdel, A., and Smets, P.: Systematic recovery of instrumental timing and phase errors using interferometric surface-waves retrieved from large-*N* seismic arrays, Geophys. J. Int., 224, 1028–1055, https://doi.org/10.1093/gji/ggaa504, 2021.

Weidle, C., Soomro, R. A., Cristiano, L., and Meier, T.: Identification of response and timing issues at permanent European broadband stations from automated data analysis, Adv. Geosci., 36, 21–25, https://doi.org/10.5194/adgeo-36-21-2013, 2013.

Yang, Y., Song, X., and Ringler, A. T.: An evaluation of the timing accuracy of global and regional seismic stations and networks, Seismol. Res. Lett., 93, 161–172, https://doi.org/10.1785/0220210232, 2022.

Yang, Y., Song, X., and Ringler, A. T.: Erratum to an evaluation of the timing accuracy of global and regional seismic stations and networks, Seismol. Res. Lett., 95, 556, https://doi.org/10.1785/0220230360, 2024.

https://doi.org/10.5194/egusphere-2026-5154
Preprint. Discussion started: 2 November 2026
© Author(s) 2026. CC BY 4.0 License.

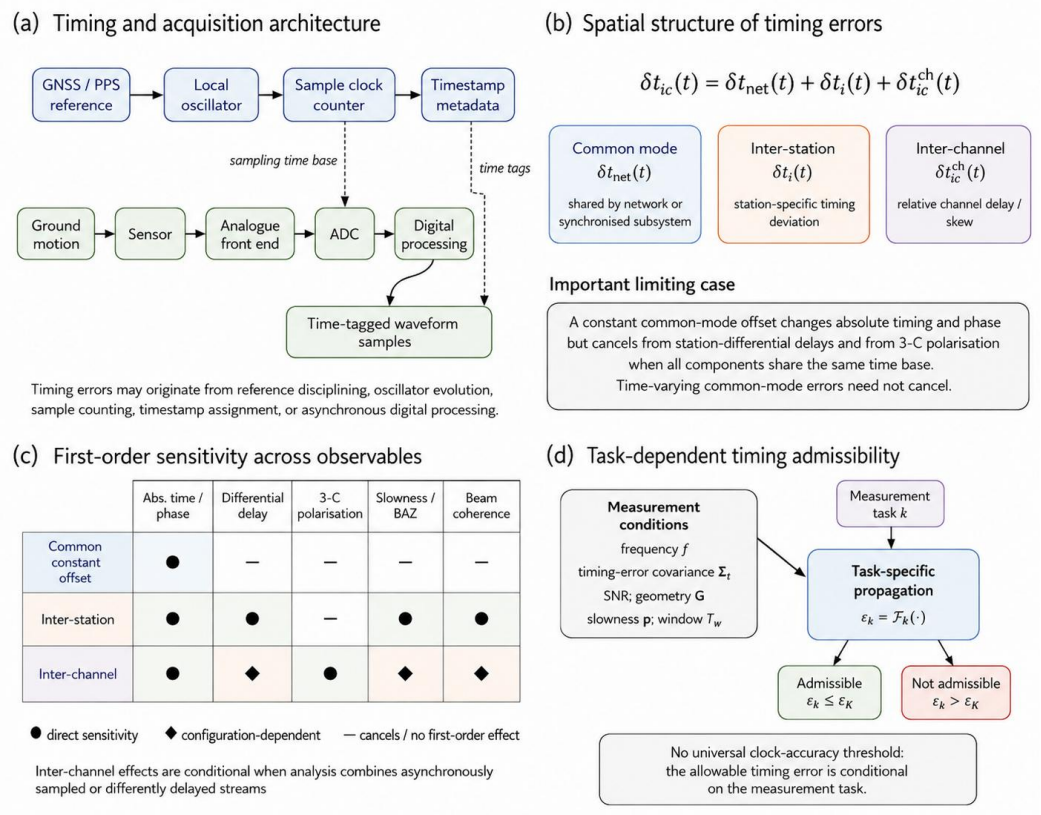


Figure 1. Spatial structure of timing errors and task-dependent timing-admissibility framework for digital seismology. (a) Timing and acquisition architecture, showing the time-reference path from GNSS/pulse-per-second PPS disciplining through the local oscillator, sample clock, and timestamp metadata, together with the seismic signal path from ground motion through the sensor, analogue front end, analogue-to-digital converter (ADC), and digital processing to time-tagged waveform samples. Timing errors may originate from reference disciplining, oscillator evolution, sample counting, timestamp assignment, or asynchronous digital processing. (b) Spatial decomposition of the timing error for channel (c) of station (i) into network- or subsystem-common, inter-station, and inter-channel contributions. A constant common-mode offset changes absolute timing and phase but cancels from station-differential delays and from three-component polarisation when all components share the same time base; time-varying common-mode clock errors need not cancel and are treated separately through the temporal clock-error model. (c) First-order sensitivity and cancellation matrix linking the principal spatial error modes to absolute timing and phase, differential delay, three-component polarisation, array slowness and backazimuth (BAZ), and coherent beamforming. The inter-station classification assumes a station-wide timing error shared by synchronously sampled three-component channels. Filled circles denote direct first-order sensitivity, diamonds denote configuration-dependent sensitivity, and dashes indicate cancellation or absence of a first-order effect under the stated limiting conditions. (d) Task-dependent timing-admissibility framework. Frequency, timing-error covariance, signal-to-noise ratio, array geometry, wavefield slowness, analysis-window duration, and the selected measurement task determine the propagated measurement error and whether it remains below a task-specific tolerance. The framework therefore replaces a universal clock-accuracy threshold with a conditional timing-admissibility criterion.

https://doi.org/10.5194/egusphere-2026-5154
Preprint. Discussion started: 2 November 2026
© Author(s) 2026. CC BY 4.0 License.

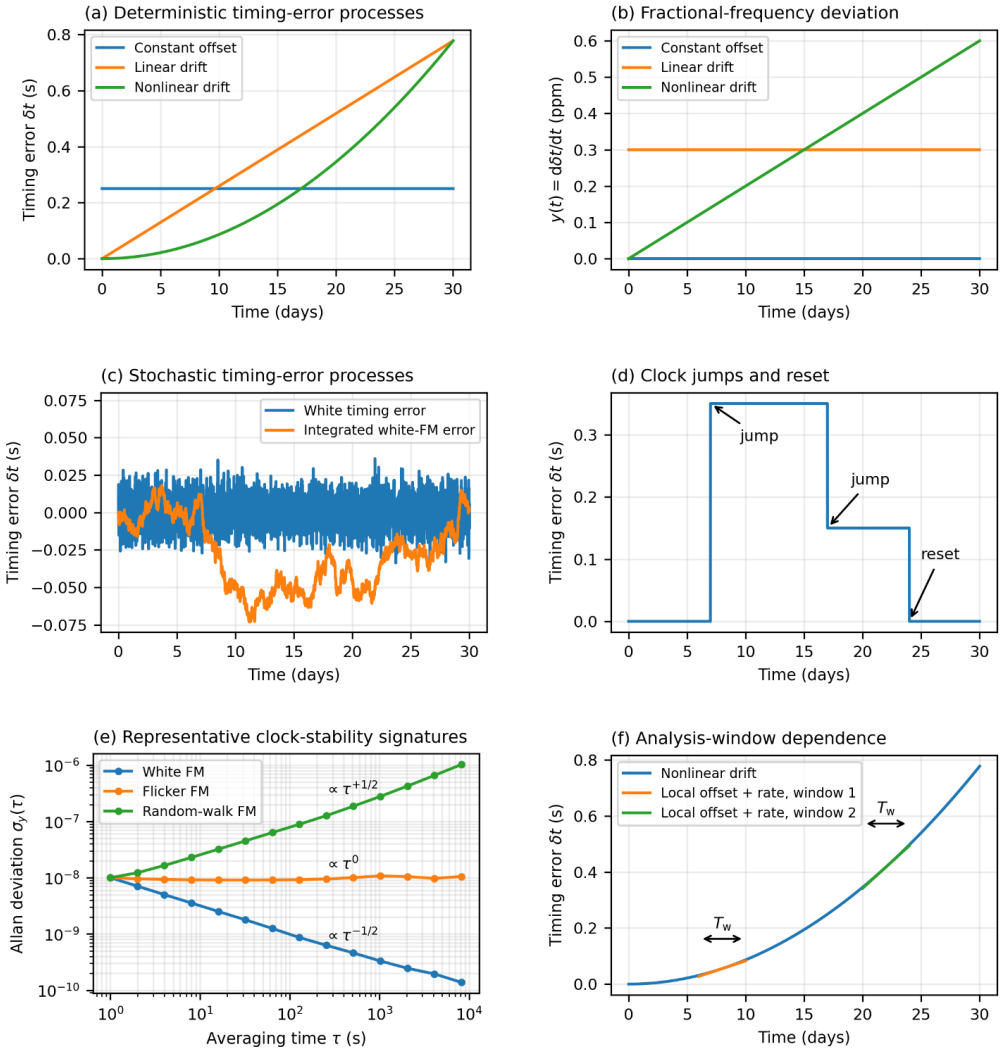


Figure 2. Temporal clock-error processes and stability characterisation used to define the synthetic timing benchmark. (a) Deterministic timing-error histories comprising a constant offset, a linear drift produced by a constant fractional-frequency error, and a nonlinear drift produced by a time-varying fractional-frequency error. (b) Corresponding fractional-frequency deviation, $y(t) = \mathrm{d}\delta t/\mathrm{d}t$. A constant timing offset has zero rate error, a linear timing drift corresponds to constant y, and the quadratic timing error shown in (a) corresponds to a linearly varying y. (c) Illustrative stochastic timing-error processes, including an uncorrelated white timing error used as a discrete surrogate for short-term timing jitter and the timing error obtained by integrating white fractional-frequency noise. (d) Piecewise-discontinuous timing history illustrating two clock jumps followed by a reset. (e) Overlapping Allan deviation for representative synthetic white-FM, flicker-FM, and random-walk-FM processes. These stability processes form an independent normalised benchmark and are not the Allan deviations of the illustrative time series shown in (c). All three are normalised to the same Allan deviation at $\tau = 1$ s to emphasise their different scale dependences rather than instrument-specific stability levels; their expected asymptotic behaviours are approximately $\sigma_y(\tau) \propto \tau^{-1/2}$, $\sigma_y(\tau) \propto \tau^{0}$, and $\sigma_y(\tau) \propto \tau^{+1/2}$, respectively. (f) Local representation of a nonlinear timing drift over finite analysis windows. Horizontal double-headed arrows indicate the full duration T_w of each window. Within a sufficiently short window, a smoothly varying clock error can be approximated by a local timing offset plus fractional-frequency error,

https://doi.org/10.5194/egusphere-2026-5154
Preprint. Discussion started: 2 November 2026
© Author(s) 2026. CC BY 4.0 License.

whereas the approximation depends on both window position and duration. All amplitudes in (a)–(d) are illustrative synthetic benchmark values and are not intended to represent specifications of any particular seismic instrument.

https://doi.org/10.5194/egusphere-2026-5154
Preprint. Discussion started: 2 November 2026
© Author(s) 2026. CC BY 4.0 License.

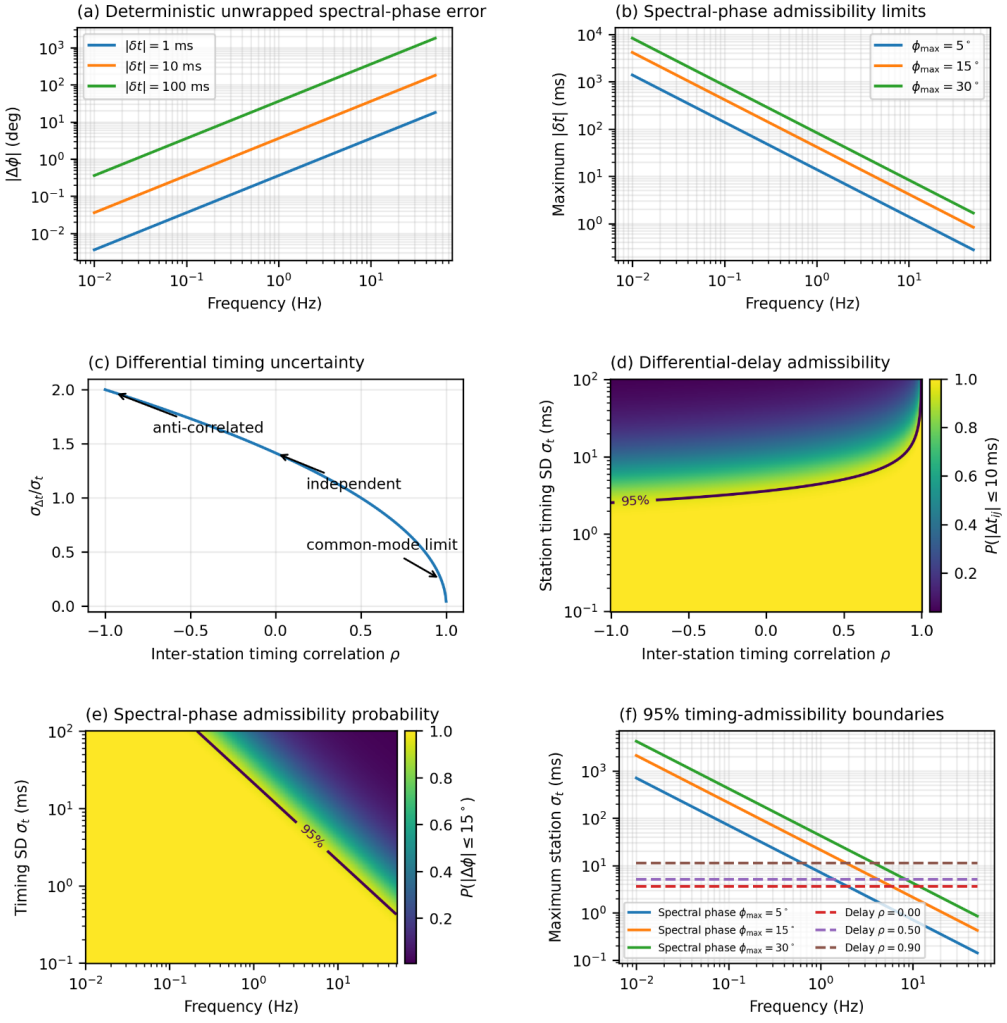


Figure 3. Frequency-dependent unwrapped spectral-phase and differential-delay admissibility under deterministic and stochastic timing errors. (a) Magnitude of the unwrapped spectral-phase error produced by fixed timing offsets of 1, 10, and 100 ms, illustrating the linear relation $|\Delta\phi| = 2\pi f|\delta t|$. The phase error is treated as unwrapped, so modulo-2π phase equivalence is not invoked. (b) Maximum deterministic timing offset compatible with illustrative unwrapped spectral-phase tolerances of 5°, 15°, and 30°. (c) Differential timing uncertainty for two stations with equal timing standard deviation σ_t and inter-station correlation ρ, for which $\sigma_{\Delta t}/\sigma_t = [2(1-\rho)]^{1/2}$. Anti-correlated station errors increase the differential uncertainty above the independent-error value $\sqrt{2}\sigma_t$, whereas increasingly common-mode errors reduce it towards zero. (d) Probability that the absolute differential timing error remains within an illustrative 10 ms tolerance as a function of station timing uncertainty and inter-station correlation; the contour denotes 95 % admissibility. (e) Probability that the magnitude of the unwrapped spectral-phase error remains within an illustrative 15° tolerance as a function of frequency and timing uncertainty; the contour again denotes 95 % admissibility. (f) Maximum station timing standard deviation compatible with 95 % admissibility. Solid curves show unwrapped spectral-phase-based limits for the three illustrative phase tolerances, whereas dashed curves show differential-delay limits for a 10 ms tolerance at three levels of inter-station timing correlation. Panels (c)–(f) describe residual zero-mean timing errors after deterministic timing bias is treated separately, and the probabilistic results in (d)–(f) assume Gaussian residual timing errors. The comparison demonstrates that the timing

https://doi.org/10.5194/egusphere-2026-5154
Preprint. Discussion started: 2 November 2026
© Author(s) 2026. CC BY 4.0 License.

requirement is jointly frequency-, task-, tolerance-, and covariance-dependent. All tolerance values are synthetic benchmark choices used to expose the structure of the admissibility problem and are not proposed as universal seismic-instrument specifications.

https://doi.org/10.5194/egusphere-2026-5154
Preprint. Discussion started: 2 November 2026
© Author(s) 2026. CC BY 4.0 License.

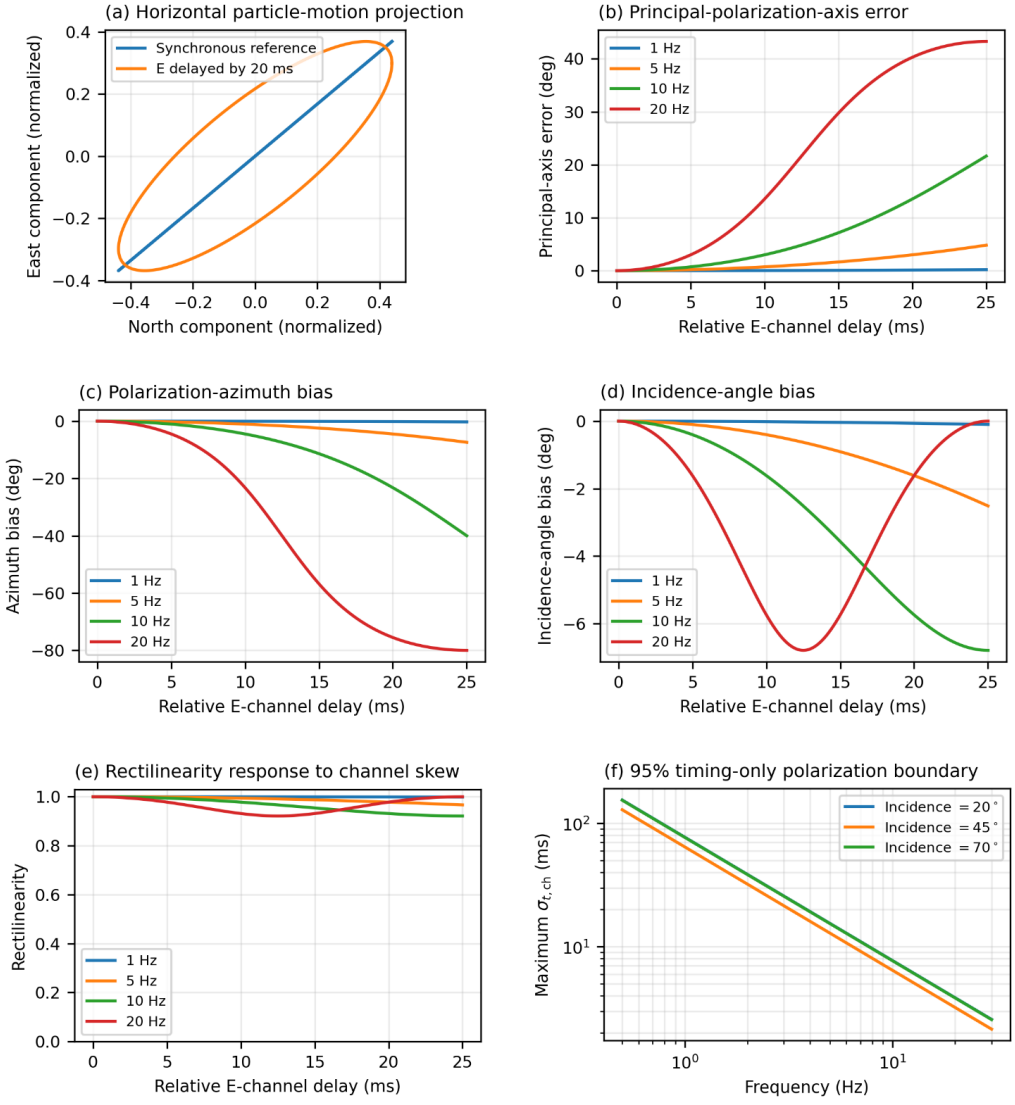


Figure 4. Polarisation distortion caused by relative inter-channel timing skew in an ideal long-window, narrow-band, noise-free three-component benchmark. A linearly polarised wavefield with reference azimuth 40° and incidence angle 35° is used in panels (a)–(e); only the E component is delayed, whereas the N and Z components retain the reference time base. (a) Horizontal particle-motion projection for the synchronous reference and for a 20 ms E-channel delay at 5 Hz. The relative delay transforms the reference linear trajectory into an apparent ellipse. (b) Angular error of the principal polarisation axis as a function of relative E-channel delay for 1, 5, 10, and 20 Hz. (c) Corresponding polarisation-azimuth bias. (d) Corresponding incidence-angle bias. The 180° ambiguity of the principal eigenvector is resolved against the known synthetic reference direction. (e) Rectilinearity response to channel skew, computed from the ordered covariance-matrix eigenvalues as $R = 1 - (\lambda_2 + \lambda_3)/(2\lambda_1)$. Rectilinearity need not decrease monotonically with timing skew: near a half-cycle relative delay, an apparently rectilinear trajectory can re-emerge while retaining an incorrect polarisation direction. Panels (b)–(e) are therefore restricted to delays of 0–25 ms, corresponding to at most one half-cycle at the highest benchmark frequency of 20 Hz; the narrow-band response continues periodically beyond this interval. (f) Maximum standard deviation of a zero-mean Gaussian relative E-channel timing error

https://doi.org/10.5194/egusphere-2026-5154
Preprint. Discussion started: 2 November 2026
© Author(s) 2026. CC BY 4.0 License.

compatible with a 95 % probability that the principal-axis angular error remains within an illustrative 5° tolerance. The boundary is defined by the first crossing of the deterministic principal-axis error threshold. Curves are shown for incidence angles of 20°, 45°, and 70° at a fixed azimuth of 40°, and therefore quantify incidence-angle dependence rather than the complete azimuth–incidence geometry. The boundary isolates timing uncertainty alone and excludes additive waveform noise, component-orientation errors, response mismatch, and other instrumental or propagation effects. Deterministic timing bias is treated separately from the residual timing uncertainty used in panel (f). All frequencies, delays, orientations, and tolerance values are synthetic benchmark choices and are not intended as universal specifications for three-component seismic systems.

https://doi.org/10.5194/egusphere-2026-5154
Preprint. Discussion started: 2 November 2026
© Author(s) 2026. CC BY 4.0 License.

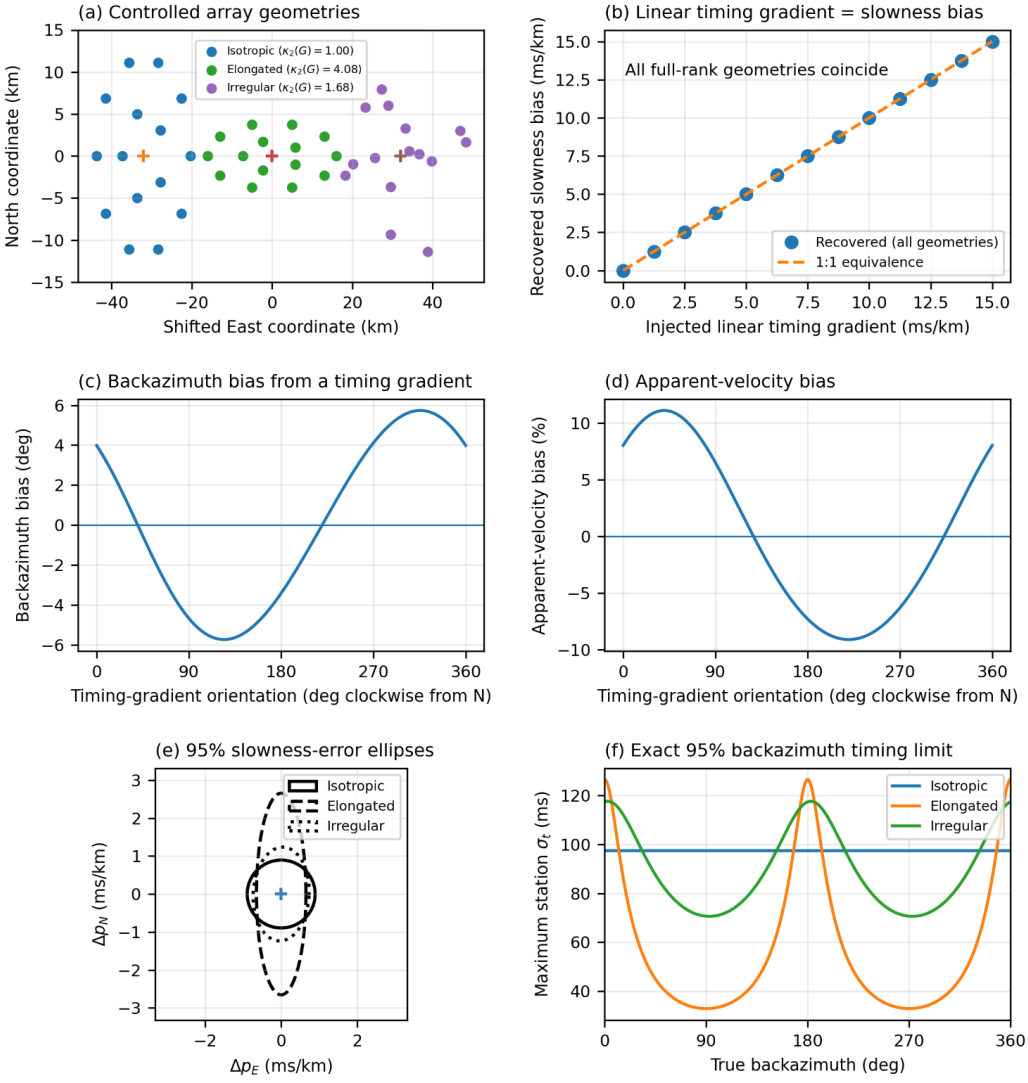


Figure 5. Analytical projection of station timing errors into horizontal slowness, backazimuth, and apparent velocity for controlled planar-array geometries. Arrival times are represented as $\mathbf{t} = t_0\mathbf{1} + \mathbf{Gp} + \boldsymbol{\delta t}$, where $\mathbf{G}$ contains station east and north coordinates and $\mathbf{p}$ is the horizontal propagation-slowness vector. Backazimuth θ is measured clockwise from North toward the source, with $\mathbf{p} = -u[\sin\theta, \cos\theta]^T$ and apparent velocity $v_{\mathrm{app}} = 1/u$. (a) Isotropic, elongated, and irregular 15-station arrays scaled to the same 10 km RMS radius; labels report the 2-norm condition number $\kappa_2(\mathbf{G})$, defined as the ratio of the largest to the smallest singular value of the centred geometry matrix. (b) Recovered slowness bias for a spatially linear station timing field. Because $\boldsymbol{\delta t} = \mathbf{Gg}$ is algebraically indistinguishable from a slowness perturbation $\mathbf{g}$, the recovered bias follows the 1:1 relation for every full-rank geometry, whereas a station-common constant offset is absorbed by the fitted intercept and produces no slowness bias. (c) Backazimuth bias produced by a linear timing gradient of fixed magnitude 8 ms km^{-1} as its orientation varies clockwise from North, for a reference horizontal slowness of 0.08 s km^{-1} and backazimuth 40°. (d) Corresponding apparent-velocity bias. The deterministic linear-gradient results in (b)–(d) are geometry-independent under the stated full-rank plane-wave model because the timing gradient lies exactly in the column space of $\mathbf{G}$. (e) Joint two-dimensional 95 % slowness-error probability regions generated by independent zero-mean Gaussian station timing errors with standard deviation

https://doi.org/10.5194/egusphere-2026-5154
Preprint. Discussion started: 2 November 2026
© Author(s) 2026. CC BY 4.0 License.

10 ms. Their size and anisotropy are controlled by array geometry through the timing-to-slowness projection operator. (f) Exact maximum station timing standard deviation compatible with a 95 % probability that the absolute backazimuth error remains within an illustrative 5° tolerance, shown as a function of true backazimuth for the three geometries at fixed 0.08 s km^{-1} slowness. The Gaussian angular-sector probability is evaluated without linearising the backazimuth transformation. Arrival-phase identification and association are assumed to remain fixed and correct; the calculated limits therefore quantify parameter-estimation admissibility after phase association rather than detection or association failure. The panel isolates timing uncertainty under the plane-wave, planar-array, equal-weight, independent-error benchmark. All geometries, timing levels, slowness values, and tolerances are synthetic choices used to expose the forward-propagation structure and are not proposed as universal array specifications.

https://doi.org/10.5194/egusphere-2026-5154
Preprint. Discussion started: 2 November 2026
© Author(s) 2026. CC BY 4.0 License.

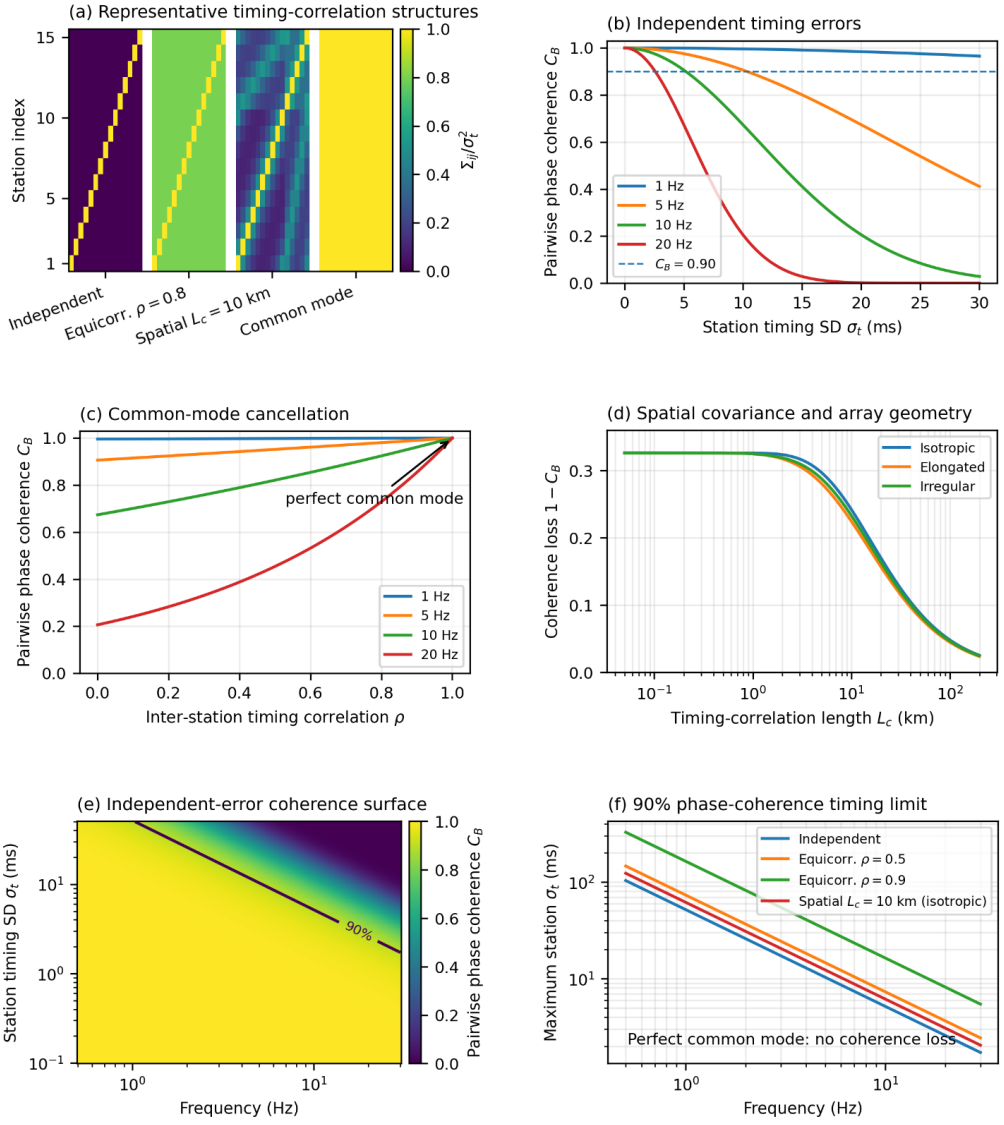


Figure 6. Timing-error covariance, beam coherence, and timing-admissibility bounds for controlled seismic arrays. For a beam steered to the correct plane-wave slowness, residual station timing errors introduce phase factors $\exp(-i2\pi f \delta t_i)$. Here, $\boldsymbol{\Sigma_t}$ denotes the inter-station covariance of the residual timing-error vector within a fixed analysis window, distinct from the temporal clock-stability characterisation in Fig. 2. For a zero-mean multivariate Gaussian timing-error vector, the expected timing-induced pairwise phase-coherence retention and the corresponding normalised beam power are given by Eqs. (39)–(40). (a) Representative normalised timing-correlation matrices for independent, equicorrelated, spatially correlated, and perfectly common-mode errors in a 15-station benchmark. (b) Expected pairwise phase coherence as a function of station timing standard deviation for independent errors at 1, 5, 10, and 20 Hz; the dashed line denotes the illustrative criterion $C_B = 0.90$. (c) Effect of inter-station equicorrelation at fixed 10 ms station timing standard deviation. Increasing common-mode content suppresses differential phase error, and perfectly common-mode timing errors preserve pairwise phase coherence at all frequencies in this timing-only model. (d) Coherence loss for an exponential spatial timing-correlation model at 10 Hz and 10 ms timing standard deviation for isotropic,

https://doi.org/10.5194/egusphere-2026-5154
Preprint. Discussion started: 2 November 2026
© Author(s) 2026. CC BY 4.0 License.

elongated, and irregular 15-station arrays having the same 10 km RMS radius. The covariance model is $\Sigma_{ij} = \sigma_t^2 \exp(-d_{ij}/L_c)$; geometry affects coherence through the distribution of inter-station separations relative to L_c. (e) Frequency–timing-uncertainty phase-coherence surface for independent station errors; the contour denotes $C_B = 0.90$. (f) Maximum station timing standard deviation compatible with the same phase-coherence criterion for independent, partially equicorrelated, and spatially correlated timing errors. The spatially correlated boundary uses $L_c = 10$ km and the isotropic benchmark geometry. A perfectly common-mode station timing error has no finite coherence-based upper bound because all stations acquire the same phase shift. The benchmark assumes correct steering, equal station weights, identical signal amplitudes, Gaussian residual timing errors, and no additive waveform noise, response mismatch, phase-identification failure, or propagation-model error. The $C_B = 0.90$ criterion and all covariance parameters are illustrative synthetic choices rather than universal array specifications.

https://doi.org/10.5194/egusphere-2026-5154
Preprint. Discussion started: 2 November 2026
© Author(s) 2026. CC BY 4.0 License.

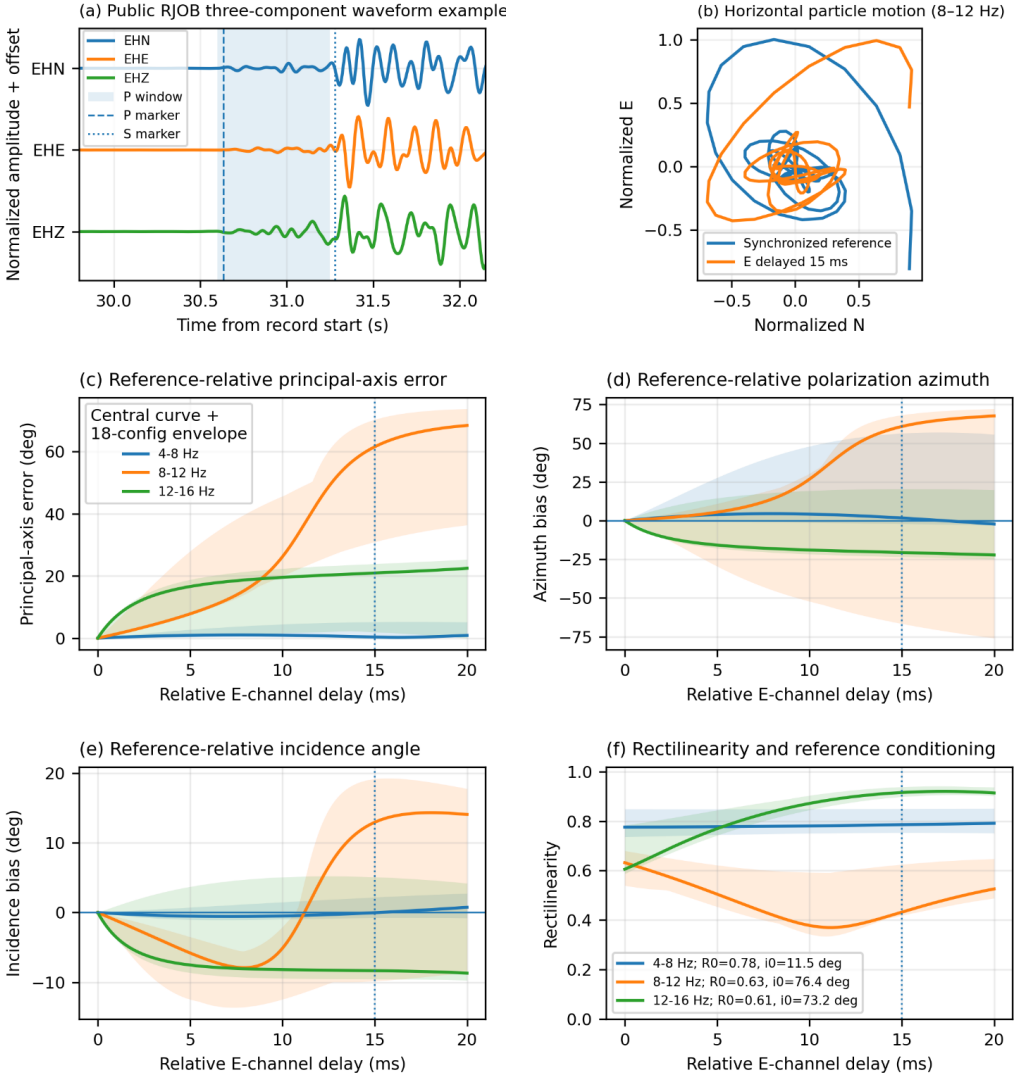


Figure 7. Controlled relative inter-channel timing perturbations of a public observational three-component waveform example. The reference waveform is the public ObsPy RJOB EHN, EHE, and EHZ example sampled at 200 Hz. The documented ObsPy autoregressive-picker values $P = 30.635$ s and $S = 31.280$ s are used only as reproducible temporal markers. The synchronised waveform is treated as the observational reference rather than as ground truth for absolute source polarisation. (a) Three-component waveform filtered from 4 to 16 Hz for display; the vertical lines mark the documented P and S markers, and the shaded interval denotes the central 30.60–31.25 s pre-S analysis window. (b) Horizontal N–E particle-motion projection in the 8–12 Hz band for the synchronised reference and after imposing a 15 ms delay on the E component alone. (c) Reference-relative angular error of the principal polarisation axis as a function of imposed E-channel delay for the 4–8, 8–12, and 12–16 Hz bands. Solid curves use the central analysis configuration (30.60–31.25 s window; Tukey $\alpha = 0.15$), whereas shaded envelopes span 18 predefined processing configurations formed by six entirely pre-S windows and Tukey α values of 0.05, 0.15, and 0.25. (d) Corresponding reference-relative polarisation-azimuth bias. Azimuth becomes coordinate-conditioned when the reference principal axis approaches the vertical and is therefore treated as secondary to the three-dimensional principal-axis error in (c). (e) Corresponding incidence-angle bias. (f) Rectilinearity; legend entries report the central-configuration

https://doi.org/10.5194/egusphere-2026-5154
Preprint. Discussion started: 2 November 2026
© Author(s) 2026. CC BY 4.0 License.

reference rectilinearity R_0 and reference incidence i_0, making polarisation conditioning explicit. The complete eigenvalue ratios are provided in the machine-readable reference-conditioning table. Before perturbation, all components are linearly detrended and processed with identical zero-phase fourth-order Butterworth filters. The selected bands satisfy an explicit filter-edge diagnostic: the radius containing 99.9 % of the two-sided zero-phase impulse-response energy is shorter than the available data margin around every analysis window. Fractional E-channel delays are imposed through a Fourier phase shift while N and Z remain unchanged. Instrument responses are not removed; pre-existing component-response and orientation characteristics are therefore held fixed between the reference and perturbed waveforms. The 180° principal-axis ambiguity is resolved against the unperturbed reference eigenvector independently for every band and processing configuration. The experiment quantifies reference-relative timing sensitivity and its processing dependence for a single public observational waveform rather than validating an absolute source-polarisation model. All imposed delays, processing bands, windows, and taper values are controlled benchmark choices.

https://doi.org/10.5194/egusphere-2026-5154
Preprint. Discussion started: 2 November 2026
© Author(s) 2026. CC BY 4.0 License.

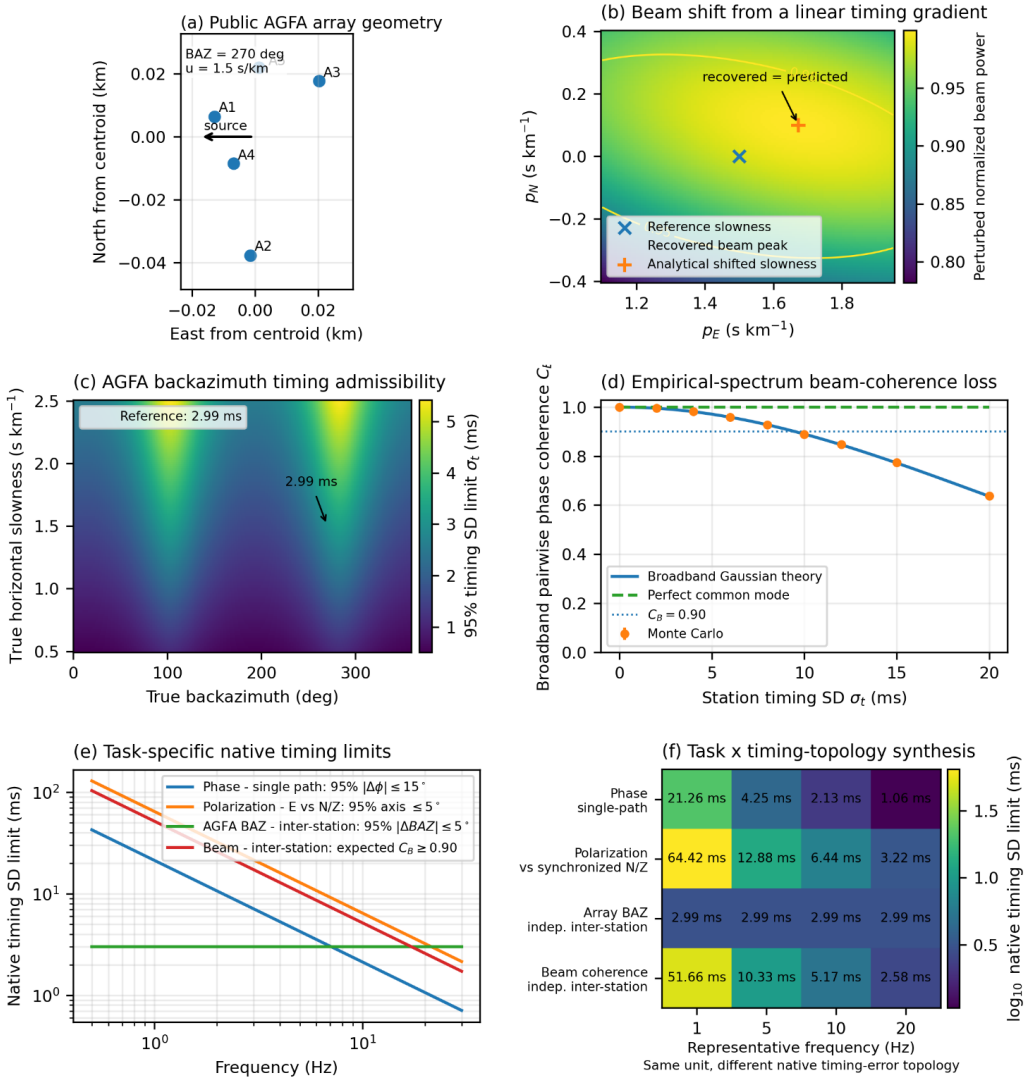


Figure 8. Public-array-geometry, empirically weighted controlled benchmark and task-topology synthesis of timing admissibility. Panels (a)–(c) use the public five-station AGFA geometry documented in the ObsPy FK-analysis tutorial, while panels (b) and (d) additionally use an empirical 4–8 Hz spectral weighting extracted from the public ObsPy RJOB EHZ waveform used in Fig. 7. The AGFA blast waveform itself is not analysed; panel (b) is therefore an empirically weighted controlled beam benchmark, whereas panel (d) is a geometry-independent broadband coherence calculation for independent and identically distributed station timing errors. (a) AGFA station geometry relative to the array centroid, with the source-directed reference backazimuth of 270° and horizontal slowness 1.5 s km^{-1}. (b) Broadband beam-power response after imposing a spatially linear station timing gradient of magnitude 0.20 s km^{-1} oriented 60° clockwise from North. Filled values show the timing-perturbed response and contours show the synchronised reference response. Symbols identify the reference slowness and the coincident analytically shifted slowness and recovered beam maximum; this coincidence is a consistency property of the full-rank plane-wave model rather than an independent observational validation. The imposed gradient corresponds to approximately 3.37 ms RMS and 9.34 ms peak-to-peak station timing variation. (c) Exact maximum independent station timing standard deviation compatible with a 95 % probability that the absolute backazimuth error remains within an illustrative 5° tolerance, shown

https://doi.org/10.5194/egusphere-2026-5154
Preprint. Discussion started: 2 November 2026
© Author(s) 2026. CC BY 4.0 License.

as a function of true backazimuth and horizontal slowness for the AGFA geometry. The sensitivity domain 0.5–2.5 s km^{-1} is a controlled subset of the slowness range used in the ObsPy FK example and avoids the singular zero-slowness limit. The marked reference point gives $\sigma_{t,\max} = 2.99$ ms at 270° and 1.5 skm^{-1}. Arrival-phase identification and association are assumed to remain fixed and correct, so these limits quantify post-association parameter-estimation admissibility. (d) Broadband timing-induced pairwise phase-coherence retention for independent zero-mean Gaussian station timing errors, with Monte Carlo estimates compared with the empirical-spectrum Gaussian expectation; perfectly common-mode station timing errors preserve inter-station phase coherence. (e) Task-specific native timing-error standard-deviation limits expressed on a common frequency axis for four illustrative criteria: 95 % probability of absolute spectral-phase error not exceeding 15° for a single-path residual timing error; 95 % probability of principal-polarisation-axis error not exceeding 5° for E-channel residual timing error relative to synchronised N/Z in the ideal Fig. 4 benchmark at incidence 45° and azimuth 40°; 95 % probability of absolute backazimuth error not exceeding 5° for independent inter-station timing errors in the marked AGFA benchmark; and the monochromatic expected pairwise beam-coherence criterion $C_B \geq 0.90$ for independent inter-station timing errors. Panel (d) is the broadband, empirically weighted counterpart of the latter criterion. (f) Topology-aware numerical synthesis at 1, 5, 10, and 20 Hz. The values may be juxtaposed because they share the same physical unit, but they are not directly commensurate estimates of a common timing-error random variable; each row retains its native timing-error topology, and the results are deliberately not collapsed into a scalar minimum envelope. All slowness values, timing perturbations, performance tolerances, and representative frequencies are controlled illustrative benchmark choices rather than universal instrument specifications.